

# Imaging of isotropic and anisotropic conductivities from power densities in three dimensions

François Monard\*      Donsub Rim†

July 25, 2018

## Abstract

We present numerical reconstructions of anisotropic conductivity tensors in three dimensions, from knowledge of a finite family of power density functionals. Such a problem arises in the coupled-physics imaging modality Ultrasound Modulated Electrical Impedance Tomography for instance. We improve on the algorithms previously derived in [9, 32] for both isotropic and anisotropic cases, and we address the well-known issue of vanishing determinants in particular. The algorithm is implemented and we provide numerical results that illustrate the improvements.

## 1 Introduction

We present a numerical implementation of reconstruction algorithms previously derived in [9, 32] for isotropic and anisotropic conductivity tensors in three spatial dimensions, from knowledge of a finite number of so-called *power density* measurements. Put in mathematical terms, the problem considered is to reconstruct  $\gamma : X \rightarrow S_3(\mathbb{R})$  a symmetric, uniformly elliptic<sup>1</sup> conductivity tensor on a given bounded domain  $X \subset \mathbb{R}^3$  from the knowledge of a finite collection of internal functionals of the form  $H_{ij}(x) = \gamma(x)\nabla u_i(x) \cdot \nabla u_j(x)$  for  $1 \leq i, j \leq J$ , where each  $u_i$  solves the conductivity equation

$$\nabla \cdot (\gamma \nabla u_i) = 0 \quad (\text{in } X), \quad u|_{\partial X} = g_i \quad (\text{prescribed}). \quad (1)$$

The inverse conductivity problem from power densities belongs to the family of *hybrid* (or *coupled-physics*) inverse problems, whose primary purpose is to design high-contrast, high-resolution medical imaging modalities by coupling two traditional imaging techniques with complementary strengths [5, 7].

---

\*Department of Mathematics, University of California, Santa Cruz CA 95064, USA. fmonard@ucsc.edu

†Department of Applied Physics and Applied Mathematics, Columbia University, New York NY, USA. dr2965@columbia.edu

<sup>1</sup> $\gamma$  is *uniformly elliptic* if there exists a constant  $\kappa \geq 1$  such that  $\kappa^{-1}|\xi|^2 \leq \gamma(x)\xi \cdot \xi \leq \kappa|\xi|^2$  for every  $x \in X$  and  $\xi \in \mathbb{R}^3$ .

Two examples of hybrid models couple conductivity imaging with ultrasonic waves, one so-called Impedance Acoustic Tomography [24], and the other, Ultrasound-Modulated Electrical Impedance Tomography [4]. These modalities ultimately lead to an inverse problem where one is provided with internal functionals (even though the method remains non-invasive) to reconstruct the internal, anisotropic conductivity. Such a problem has received much attention over the past few years, both in theoretical and numerical aspects [21, 9, 13, 26, 32, 30, 31, 10, 15, 3, 17]. In particular, the first author’s prior work on the topic has consisted of the derivation of explicit reconstruction algorithms for the non-linear problem in all dimensions  $d \geq 2$ , and the analysis of their stability. These results serve as a justification that power density measurements show much promise in their ability to give access to conductivities at higher resolution than from classical Dirichlet-to-Neumann data, and furthermore give access to anisotropic features which are traditionally unavailable in the classical Calderón’s problem.

Inverse conductivity problems share many similarities with inverse elasticity problems [8, 27, 14, 23], and some of the current framework also applies there as well, see [14]. Other internal functionals for inverse conductivity may be considered, for instance *current densities*, see [22, 38, 36, 35, 12, 11, 34].

Implementations often use iterative methods as in [4, 15, 25], for which finding a good initial guess can be crucial. The approach presented here consists in implementing explicit inversion algorithms, which may either provide satisfactory reconstructions in some cases, or a good initial guess for further improvements in others. Previous implementations in two dimensions were presented in [30] and we now present a three-dimensional implementation. In this problem, the transition from two to three spatial dimensions requires additional technical considerations, even if one ignores the issue of computational cost.

- In the isotropic case where one must reconstruct a function  $R : X \rightarrow SO(3)$  by integration of a dynamical system along curves, a choice needs to be made on how to parameterize  $SO(3)$ , involving a number of parameters between 3 and 9. Too few parameters (3: the Euler angles) lead to singularity issues not due to the actual problem but to the parameterization, see [37]; too many parameters (9, the full matrix) increases redundancy, computational cost and complexity of the dynamical system to be integrated. In this article, we use unit quaternions  $\mathbb{H}$ , a 4-parameter family describing  $SO(3)$  non-singularly. This description gives a good dimensionality tradeoff, moreover computations below show that the dynamical system parameterized in that way admits a rather symmetric form, easier to implement than the previously derived system for the 9-parameter rotation matrix. While the correspondence  $\mathbb{H} \rightarrow SO(3)$  is 2-to-1, this is the price to pay for using a non-singular parameterization of  $SO(3)$ , and in fact does not cause specific issues in the implementation.
- The validity of the reconstruction algorithms comes with conditions on the boundary conditions  $g_i$ , which are easy to satisfy in two dimensions, much less obvious in three [1, 20, 10]. In particular, two issues associated with this are: (i) how to find boundary

conditions satisfying the validity conditions; (ii) if more than the minimal number of solutions is needed, how does one efficiently determine which set works locally, and how does one combine the local reconstructions into a global one? While (i) is a difficult theoretical question which continues to receive attention and is not the focus of the present article, we address (ii) as follows: in [9], it was suggested to decompose the domain and patch local reconstructions together, but we will give a way to do this globally at once, allowing for more efficiency in the reconstruction process.

**Outline.** We first present in Section 2 a summary of the problems considered, their dimension and the existing approaches, before discussing in Section 3 the derivation of a reconstruction algorithm in the isotropic case, making use of quaternion algebra. We then adapt in Section 4 the reconstruction algorithms for anisotropic tensors to three dimensions. The numerical simulations are presented in Section 5, and some concluding remarks are provided in Section 6.

## 2 Summary of problems considered and existing approaches

We briefly recall the results from [9, 31, 30, 32, 13, 29], and we will build upon them. The analysis there consists in finding a minimal set of functionals for which reconstructions algorithms can be derived, with stability estimates in optimal spaces. For such analyses, it is natural to consider decomposing an anisotropic conductivity  $\gamma$  into the product  $\gamma = \tau\tilde{\gamma}$  with  $\tau$  a scalar function and  $\tilde{\gamma}$  a tensor satisfying  $\det \tilde{\gamma} = 1$ . Then the following three settings have been considered.

- (1) Reconstruction of an isotropic ( $\tilde{\gamma} = Id$ ) conductivity.  $\tau$  is usually denoted  $\sigma$  in this case.
- (1') In the anisotropic case, reconstruction of the scalar  $\tau$  assuming knowledge of  $\tilde{\gamma}$ .
- (2) In the anisotropic case, reconstruction of  $\tilde{\gamma}$ , then  $\tau$ .

Problem (1') is a generalization of Problem (1), of same dimensionality and resolution approach. Incorporating the presence of a non-trivial  $\tilde{\gamma}$  to solve (1') is addressed in [32, Sec. 3.1] and will not be further addressed in the present article.

### 2.1 Local reconstruction algorithms

We recall the results in any dimension  $n \geq 2$ .

**Local resolution of Problem (1).** See, e.g., [9, 31]. Suppose  $X' \subset X$  and assume that  $n$  solutions  $u_1, \dots, u_n$  of (1) (with associated power densities  $\{H_{ij}\}_{1 \leq i \leq j \leq n}$ ) satisfy

$$\inf_{x \in X'} \det(\nabla u_1(x), \dots, \nabla u_n(x)) \geq c_0 > 0. \quad (2)$$

Then one may reconstruct  $\sigma|_{X'}$  in Problem (1) up to a constant, from  $\{H_{ij}|_{X'}\}_{1 \leq i \leq j \leq n}$  with a  $W^{1,\infty} \rightarrow W^{1,\infty}$  stability estimate, see [31, Theorem 2.3]. In a nutshell, the quantities  $\nabla u_1, \dots, \nabla u_n$  are known from data up to an unknown rotation matrix  $R : \Omega \rightarrow SO(n)$ , and

the approach consists in deriving explicit equations for the full gradients  $\nabla \log \sigma$  and  $\nabla R$  as functions of  $R$  and the known data. Such equations then turn into dynamical systems along any desired integration curve, allowing the reconstruction of  $\sigma$  along a family of curves covering  $X'$ , see Section 3 for details. An alternate reconstruction approach was also proposed in [31, Section 5] involving solving a coupled elliptic system, not covered further here.

**Local resolution of Problem (2).** See, e.g., [30, 32, 13]. To address Problem (2), a family  $(u_1, \dots, u_n)$  satisfying (2) needs to be augmented with additional solutions, call them  $(v_1, \dots, v_m)$ , with  $m$  to be determined. For each additional solution  $v_j$ , the power densities  $\{\gamma \nabla u_i \cdot \nabla v_j\}_{i=1}^n$  can be exploited to bring potentially  $1 + n(n-1)/2$  pointwise linear constraints on  $\tilde{\gamma}$  in the form “ $\text{tr}(M_{jp}(\mathbf{x})\tilde{\gamma}(\mathbf{x})) = 0$ ”, where  $\{M_{jp}(\mathbf{x})\}_{p=1}^{1+n(n-1)/2}$  are matrices known from power densities. If  $m$  is then chosen large enough, and if the family

$$\{M_{jp}(\mathbf{x}), \quad 1 \leq j \leq m, \quad 1 \leq p \leq 1 + n(n-1)/2\}$$

spans the hyperplane  $\{\tilde{\gamma}(\mathbf{x})\}^\perp$  of dimension  $n^2 - 1$  in  $M_n(\mathbb{R})$  at every point of  $X'$ , then one may reconstruct  $\tilde{\gamma}$  pointwise by choosing a normal to that hyperplane. Such reconstructibility conditions can be formulated as a constraint of the form

$$\inf_{\mathbf{x} \in X'} \mathcal{P}(\{H_{ij}(\mathbf{x}), \nabla H_{ij}(\mathbf{x})\}_{1 \leq i \leq j \leq n+m}) \geq c > 0, \quad (3)$$

with  $\mathcal{P}$  a polynomial, see [32, Eq. (11)]. When (3) is satisfied, then  $\tilde{\gamma}|_{X'}$  can be reconstructed pointwise, with  $L^\infty$  norm stably controlled by the  $W^{1,\infty}$  norm of the power densities, as proved in [32, Theorem 2.7]. Note that this loss of one derivative was shown to be optimal in [13]. Once  $\tilde{\gamma}$  is reconstructed  $\tau$  can in turn be reconstructed, either as in Problem (1') (involving a dynamical approach similar to Problem (1)), or more directly as the additional data also allows for more efficient reconstruction of  $\tau$  (i.e., no dynamical system required), see Section 4 for details.

Now considering the case  $n = 3$ , we see that the reconstructibility condition (3) can in principle be satisfied with only 2 additional solutions (since they generate 8 orthogonality constraints in a 9-dimensional space), hence the name of 3 + 2 algorithm in Section 4.2 below.

## 2.2 From local to global

In light of these local algorithms, one may wonder whether conditions (2) and (3) can hold globally on  $X$  by choosing appropriate solutions  $(u_1, \dots, u_n, v_1, \dots, v_m)$ . The answer to this question is well-understood and positive in two dimensions [2]. In higher dimensions, it holds in a few cases including tensors close enough to constant (see [32, Theorem 2.8]), yet the question is generally open, including counterexamples [1, 20, 21]. Thus in three dimensions, it is currently more reasonable to think of a strategy which patches together local reconstructions, by covering

$X$  with open subdomains  $X_1, \dots, X_N$  and finding solutions satisfying conditions (2) and (3) on each  $X_j$  which guarantee reconstructibility of  $\gamma$  on each  $X_j$ . That such a scenario is possible can be proved under mild regularity assumptions on  $\gamma$  and the Runge approximation property (see [32, Theorem 2.5]).

A first patching approach was first described in [9, Section 5.2], requiring to keep track of (i) the covering, and (ii) which set of solutions satisfies conditions (2)-(3) on which subdomain. We derive an approach below which does not require keeping track of such a covering explicitly, and derives global equations to reconstruct the unknowns all at once. Such an approach implicitly exploits the fact that, given a family of solutions, conditions (2) and (3) hold locally for some subfamily of these solutions. See Section 4.3 for detail.

### 3 Isotropic reconstructions from 3 solutions

We now recall the derivation of the reconstruction for the isotropic case, following, e.g., [9]. Consider the reconstruction of a scalar conductivity  $\sigma$  from knowledge of power densities  $H_{ij} = \sigma \nabla u_i \cdot \nabla u_j$  for  $1 \leq i, j \leq 3$  corresponding to three solutions

$$\nabla \cdot (\sigma \nabla u_j) = 0 \quad (\text{in } X), \quad u_j|_{\partial X} = g_j \quad (\text{prescribed}), \quad 1 \leq j \leq 3,$$

such that  $(\nabla u_1, \nabla u_2, \nabla u_3)$  is linearly independent at every point of an open subset  $\Omega \subset X$ . Define  $S_i := \sqrt{\sigma} \nabla u_i$ ,  $1 \leq i \leq 3$ , whose inner products are known since  $H_{ij} = \langle S_i, S_j \rangle$ , and satisfy the PDEs

$$\nabla \cdot S_i + F \cdot S_i = 0, \quad \nabla \times S_i - F \times S_i = 0, \quad F := \frac{1}{2} \nabla \log \sigma, \quad 1 \leq i \leq 3.$$

Let  $S$  be the  $M_3(\mathbb{R})$ -valued matrix with columns  $(S_1, S_2, S_3)$ . Executing a QR decomposition on  $S$ , we define an  $SO(3)$ -valued function  $R = ST^T$ , with transition matrix (known from power densities)

$$T = \{t_{ij}\}_{1 \leq i, j \leq 3} = \begin{bmatrix} H_{11}^{-\frac{1}{2}} & 0 & 0 \\ -H_{12}H_{11}^{-\frac{1}{2}}d^{-1} & H_{11}^{\frac{1}{2}}d^{-1} & 0 \\ (H_{12}H_{23} - H_{22}H_{13})(dD)^{-1} & (H_{12}H_{13} - H_{11}H_{23})(dD)^{-1} & dD^{-1} \end{bmatrix}$$

with  $d := (H_{11}H_{22} - H_{12}^2)^{\frac{1}{2}}$  and  $D = (\det H)^{\frac{1}{2}}$ . Denoting  $t^{ij}$  the entries of  $T^{-1}$ , we further define for  $1 \leq i, k \leq 3$

$$V_{ik} := (\nabla t_{ij})t^{jk}, \quad V_{ik}^s = \frac{1}{2}(V_{ik} + V_{ki}), \quad V_{ik}^a := \frac{1}{2}(V_{ik} - V_{ki}). \quad (4)$$

Then the PDEs for  $(S_1, S_2, S_3)$  may turn into PDEs for  $(R_1, R_2, R_3)$ , the columns of the  $R$  matrix, given by

$$\nabla \cdot R_i = V_{ik} \cdot R_k - F \cdot R_i, \quad \nabla \times R_i = V_{ik} \times R_k + F \times R_i, \quad i = 1, 2, 3.$$

Out of this system, we derive in [9, Eq. (18)] the equation

$$F = \frac{1}{2} \nabla \log \sigma = \frac{1}{6} \nabla \log \det H + \frac{2}{3} \langle V_{ij}^s, R_i \rangle R_j, \quad (5)$$

as well as, for  $m, i = 1, 2, 3$  (see [31, Eq. (44)]),

$$\partial_m R_i = \langle \mathbf{e}_m, V_{ik}^a \rangle R_k - \langle R_k, \mathbf{e}_m \rangle V_{ik}^s + \langle V_{jk}^s, R_i \rangle \langle R_k, \mathbf{e}_m \rangle R_j + \langle F, R_i \rangle \mathbf{e}_m - \langle R_i, \mathbf{e}_m \rangle F, \quad (6)$$

with  $(\mathbf{e}_1, \mathbf{e}_2, \mathbf{e}_3)$  the canonical basis of  $\mathbb{R}^3$ .

The system (5)-(6) can be viewed as a closed first-order (over-determined) system for  $(\sigma, R)$  which can then be integrated along a family of curves through the domain (all curves along a coordinate axis for instance). The function  $\mathbf{x} \mapsto R(\mathbf{x})$  is an  $SO(3)$ -valued function, and, as mentioned in the Introduction, we first need to find a good parameterization of  $R$  in order to setup a proper dynamical system along curves. We choose the quaternionic chart as it is nowhere singular, and we now explain how to set up the corresponding dynamical system. In Section 3.1, we recall some general properties of quaternions, and then elaborate on how we may lift a differential of an  $SO(3)$ -valued function into the differential of a smooth quaternionic lift of it. We use this in Section 3.2, to turn the differential system (5)-(6) for  $(\sigma, R)$  into a differential system for  $(\sigma, q)$ , with  $q$  a quaternionic lift of  $R$ . Finally, we describe in Section 3.3 how to implement the latter system.

### 3.1 Quaternionic algebra

Real quaternions is the four-dimensional vector space spanned by  $(1, \mathbf{e}_1, \mathbf{e}_2, \mathbf{e}_3)$  equipped with the additional non-commutative multiplication “ $\cdot$ ”, for which 1 is the unit and the other basis elements satisfy  $\mathbf{e}_i \cdot \mathbf{e}_i = -1$  for  $i = 1, 2, 3$  as well as

$$\mathbf{e}_1 \cdot \mathbf{e}_2 = -\mathbf{e}_2 \cdot \mathbf{e}_1 = \mathbf{e}_3, \quad \mathbf{e}_2 \cdot \mathbf{e}_3 = -\mathbf{e}_3 \cdot \mathbf{e}_2 = \mathbf{e}_1, \quad \mathbf{e}_3 \cdot \mathbf{e}_1 = -\mathbf{e}_1 \cdot \mathbf{e}_3 = \mathbf{e}_2.$$

The subspace  $\mathbb{R}1$  is the space of “scalars” while the copy of  $\mathbb{R}^3$  spanned by  $(\mathbf{e}_1, \mathbf{e}_2, \mathbf{e}_3)$  is called “vectors”. For two vectors  $u, v$  viewed as quaternions with no scalar part, one may easily establish that

$$u \cdot v = -\langle u, v \rangle + u \times v,$$

where  $\langle \cdot, \cdot \rangle$  is the standard Euclidean dot product and  $\times$  is the cross product. In what follows, we will use the cross product notation for two quaternions only if they have no scalar part. In particular, we can write the identity

$$u \times v = \frac{1}{2}(u \cdot v - v \cdot u).$$

A quaternion is thus of the form  $q = q_0 + q_1\mathbf{e}_1 + q_2\mathbf{e}_2 + q_3\mathbf{e}_3$  with real components. We define its conjugate  $\bar{q} := q_0 - q_1\mathbf{e}_1 - q_2\mathbf{e}_2 - q_3\mathbf{e}_3$  with the property that  $q \cdot \bar{q} = \bar{q} \cdot q = |q|^2 := q_0^2 + q_1^2 + q_2^2 + q_3^2$ . Vectors viewed as quaternions satisfy  $\bar{v} = -v$ .

Unit quaternions  $\mathbb{H} = \{q : |q| = 1\}$  are isomorphic to  $\mathbb{S}^3$  and form a 2-to-1 covering of  $SO(3)$  via the following map: for  $q$  with  $|q| = 1$  and  $v = v_1\mathbf{e}_1 + v_2\mathbf{e}_2 + v_3\mathbf{e}_3$  a vector, the linear map of  $v$  defined as  $T_q v := q \cdot v \cdot \bar{q}$  has no scalar part (i.e., defines a vector) and has the same norm as  $v$ , as can be seen from the identity

$$|q \cdot v \cdot \bar{q}|^2 = q \cdot v \cdot \bar{q} \cdot \overline{q \cdot v \cdot \bar{q}} = -q \cdot v \cdot \bar{q} \cdot q \cdot v \cdot \bar{q} = q \cdot |v|^2 \cdot \bar{q} = |v|^2.$$

It is also orientation-preserving, as can be seen from the identity

$$(q \cdot \mathbf{e}_1 \cdot \bar{q}) \times (q \cdot \mathbf{e}_2 \cdot \bar{q}) = q \cdot \mathbf{e}_3 \cdot \bar{q}.$$

One may then construct an  $SO(3)$  valued function  $(R_1, R_2, R_3)$  out of any  $\mathbb{H}$ -valued function by setting  $R_i := q \cdot \mathbf{e}_i \cdot \bar{q}$  for  $i = 1, 2, 3$ . The fact that quaternions form a 2-to-1 covering of  $SO(3)$  follows from the observation that  $T_q = T_{-q}$ . Note also that  $T_q^{-1} = T_q^* = T_{\bar{q}}$ . In particular, we have that

$$\langle u, q \cdot v \cdot \bar{q} \rangle = \langle \bar{q} \cdot u \cdot q, v \rangle,$$

for any pair of vectors  $(u, v)$ .

We now start from an  $SO(3)$ -valued function  $t \mapsto R(t) \in SO(3)$  depending differentiably on a parameter  $t$ , then explain how, if  $q(t)$  is a differentiable quaternionic lift of  $R(t)$  in the sense that  $R_j = q \cdot \mathbf{e}_j \cdot \bar{q}$  for  $j = 1, 2, 3$ , we can determine  $\partial_t q$  from  $\partial_t R$ .

**Lemma 3.1.** *If  $R(t)$  is a differentiable  $SO(3)$ -valued function and  $q(t)$  is a differentiable quaternionic lift of it, then*

$$2\bar{q} \cdot \partial_t q = \langle \bar{q} \cdot \partial_t R_2 \cdot q, \mathbf{e}_3 \rangle \mathbf{e}_1 + \langle \bar{q} \cdot \partial_t R_3 \cdot q, \mathbf{e}_1 \rangle \mathbf{e}_2 + \langle \bar{q} \cdot \partial_t R_1 \cdot q, \mathbf{e}_2 \rangle \mathbf{e}_3. \quad (7)$$

*Proof of Lemma 3.1.* Note that  $\bar{q} \cdot \partial_t q$  is a vector, as by direct calculation  $(\bar{q} \cdot \partial_t q)_0 = \frac{1}{2} \partial_t |q|^2 = 0$ . Moreover, since  $\partial_t(q \cdot \bar{q}) = 0$ , we have that  $\partial_t \bar{q} = -\bar{q} \cdot \partial_t q \cdot \bar{q}$ . We have

$$\begin{aligned} \partial_t R_i &= \partial_t(q \cdot \mathbf{e}_i \cdot \bar{q}) \\ &= \partial_t q \cdot \mathbf{e}_i \cdot \bar{q} + q \cdot \mathbf{e}_i \cdot \partial_t \bar{q} \\ &= \partial_t q \cdot \mathbf{e}_i \cdot \bar{q} - q \cdot \mathbf{e}_i \cdot \bar{q} \cdot \partial_t q \cdot \bar{q} \\ &= q \cdot (\bar{q} \cdot \partial_t q \cdot \mathbf{e}_i - \mathbf{e}_i \cdot \bar{q} \cdot \partial_t q) \cdot \bar{q}, \end{aligned}$$

and thus

$$\frac{1}{2} \bar{q} \cdot \partial_t R_i \cdot q = \frac{1}{2} (\bar{q} \cdot \partial_t q \cdot \mathbf{e}_i - \mathbf{e}_i \cdot \bar{q} \cdot \partial_t q) = (\bar{q} \cdot \partial_t q) \times \mathbf{e}_i, \quad i = 1, 2, 3.$$

Equation (7) then follows by using the fact that any vector  $u$  can be recovered from  $u \times \mathbf{e}_i$  via the formula

$$u = \langle u \times \mathbf{e}_2, \mathbf{e}_3 \rangle \mathbf{e}_1 + \langle u \times \mathbf{e}_3, \mathbf{e}_1 \rangle \mathbf{e}_2 + \langle u \times \mathbf{e}_1, \mathbf{e}_2 \rangle \mathbf{e}_3.$$

Lemma 3.1 is proved.  $\square$

In what follows,  $R$  will depend on three coordinates and Lemma 3.1 provides the basis for computing partial derivatives of the lift  $q$  of  $R$ .

### 3.2 Dynamical system for $q$

We now use Lemma 3.1 to derive a dynamical system for  $(\sigma, q)$ , with  $q$  a quaternionic lift of  $R$ , from the dynamical system for  $(\sigma, R)$  in (5)-(6).

**Theorem 3.2** (Dynamical system for  $q$ ). *Let  $(\sigma, R)$  satisfy equations (5)-(6) and let  $q$  be a quaternion-valued function such that  $R_j = q \cdot \mathbf{e}_j \cdot \bar{q}$  for  $j = 1, 2, 3$ . Then for any  $1 \leq m \leq 3$ ,  $q$  satisfies the dynamical system*

$$\partial_m q = \frac{1}{2}(q \cdot \mathbf{a}^m(q) + \mathbf{b}^m \cdot q), \quad \mathbf{b}^m := \left( \frac{1}{6} \nabla \log \det H \right) \times \mathbf{e}_m, \quad (8)$$

and where, denoting  $T_{\bar{q}}\mathbf{e}_m = \mathbf{t} = t_1\mathbf{e}_1 + t_2\mathbf{e}_2 + t_3\mathbf{e}_3$ , the vector  $\mathbf{a}^m = a_1^m\mathbf{e}_1 + a_2^m\mathbf{e}_2 + a_3^m\mathbf{e}_3$  reads

$$\begin{aligned} a_1^m &= \langle \mathbf{e}_m, V_{23}^a \rangle + t_k((T_{\bar{q}}V_{3k}^s)_2 - (T_{\bar{q}}V_{2k}^s)_3) + \frac{2}{3}((T_{\bar{q}}V_{2k}^s)_k t_3 - (T_{\bar{q}}V_{3k}^s)_k t_2), \\ a_2^m &= \langle \mathbf{e}_m, V_{31}^a \rangle + t_k((T_{\bar{q}}V_{1k}^s)_3 - (T_{\bar{q}}V_{3k}^s)_1) + \frac{2}{3}((T_{\bar{q}}V_{3k}^s)_k t_1 - (T_{\bar{q}}V_{1k}^s)_k t_3), \\ a_3^m &= \langle \mathbf{e}_m, V_{12}^a \rangle + t_k((T_{\bar{q}}V_{2k}^s)_1 - (T_{\bar{q}}V_{1k}^s)_2) + \frac{2}{3}((T_{\bar{q}}V_{1k}^s)_k t_2 - (T_{\bar{q}}V_{2k}^s)_k t_1), \end{aligned} \quad (9)$$

where any repeated index is being summed over.

*Proof of Theorem 3.2.* Fix  $1 \leq m \leq 3$ . Using Lemma 3.1 with  $\partial_t \equiv \partial_m$ , we read

$$2\bar{q} \cdot \partial_m q = \langle \bar{q} \cdot \partial_m R_2 \cdot q, \mathbf{e}_3 \rangle \mathbf{e}_1 + \langle \bar{q} \cdot \partial_m R_3 \cdot q, \mathbf{e}_1 \rangle \mathbf{e}_2 + \langle \bar{q} \cdot \partial_m R_1 \cdot q, \mathbf{e}_2 \rangle \mathbf{e}_3. \quad (10)$$

Using that  $R_i = q \cdot \mathbf{e}_i \cdot \bar{q}$  for  $1 \leq i \leq 3$ , Equation (6) becomes

$$\begin{aligned} \bar{q} \cdot \partial_m R_i \cdot q &= \langle \mathbf{e}_m, V_{ik}^a \rangle \mathbf{e}_k - \langle q \cdot \mathbf{e}_k \cdot \bar{q}, \mathbf{e}_m \rangle \bar{q} \cdot V_{ik}^s \cdot q + \langle V_{jk}^s, q \cdot \mathbf{e}_i \cdot \bar{q} \rangle \langle q \cdot \mathbf{e}_k \cdot \bar{q}, \mathbf{e}_m \rangle \mathbf{e}_j \dots \\ &\quad + \langle F, q \cdot \mathbf{e}_i \cdot \bar{q} \rangle \bar{q} \cdot \mathbf{e}_m \cdot q - \langle q \cdot \mathbf{e}_i \cdot \bar{q}, \mathbf{e}_m \rangle \bar{q} \cdot F \cdot q. \end{aligned}$$

We now use the notation  $(u)_i = \langle u, \mathbf{e}_i \rangle$  and the identity  $\langle T_{\bar{q}}u, v \rangle = \langle u, T_{\bar{q}}v \rangle$  to rewrite

$$\begin{aligned} \bar{q} \cdot \partial_m R_i \cdot q &= \langle \mathbf{e}_m, V_{ik}^a \rangle \mathbf{e}_k + (T_{\bar{q}}\mathbf{e}_m)_k ((T_{\bar{q}}V_{jk}^s)_i \mathbf{e}_j - T_{\bar{q}}V_{ik}^s) + ((T_{\bar{q}}F)_i T_{\bar{q}}\mathbf{e}_m - (T_{\bar{q}}\mathbf{e}_m)_i T_{\bar{q}}F) \\ &= \langle \mathbf{e}_m, V_{ik}^a \rangle \mathbf{e}_k + (T_{\bar{q}}\mathbf{e}_m)_k ((T_{\bar{q}}V_{jk}^s)_i \mathbf{e}_j - T_{\bar{q}}V_{ik}^s) + (T_{\bar{q}}F \times T_{\bar{q}}\mathbf{e}_m) \times \mathbf{e}_i. \end{aligned}$$

We now construct the right hand side of (10) by summing the equations above appropriately. Summing over the first terms above gives directly

$$\langle \mathbf{e}_m, V_{23}^a \rangle \mathbf{e}_1 + \langle \mathbf{e}_m, V_{31}^a \rangle \mathbf{e}_2 + \langle \mathbf{e}_m, V_{12}^a \rangle \mathbf{e}_3. \quad (11)$$

Summing over the middle terms gives

$$(T_{\bar{q}}\mathbf{e}_m)_k [((T_{\bar{q}}V_{3k}^s)_2 - (T_{\bar{q}}V_{2k}^s)_3) \mathbf{e}_1 + ((T_{\bar{q}}V_{1k}^s)_3 - (T_{\bar{q}}V_{3k}^s)_1) \mathbf{e}_2 + ((T_{\bar{q}}V_{2k}^s)_1 - (T_{\bar{q}}V_{1k}^s)_2) \mathbf{e}_3] \quad (12)$$

Summing the last terms gives directly  $T_{\bar{q}}F \times T_{\bar{q}}\mathbf{e}_m$ . Now equation (5) becomes

$$F = G + \frac{2}{3} \langle V_{ij}^s, q \cdot \mathbf{e}_i \cdot \bar{q} \rangle q \cdot \mathbf{e}_j \cdot \bar{q}, \quad G := \frac{1}{6} \nabla \log \det H,$$

so that the  $T_{\bar{q}}F \times T_{\bar{q}}\mathbf{e}_m$  term becomes

$$T_{\bar{q}}F \times T_{\bar{q}}\mathbf{e}_m = T_{\bar{q}}G \times T_{\bar{q}}\mathbf{e}_m + \frac{2}{3} (T_{\bar{q}}V_{ij}^s)_i \mathbf{e}_j \times T_{\bar{q}}\mathbf{e}_m. \quad (13)$$

Summing (11), (12) and (13) and equating with  $2\bar{q} \cdot \partial_m q$ , we arrive at

$$2\bar{q} \cdot \partial_m q = \mathbf{a}^m + T_{\bar{q}}G \times T_{\bar{q}}\mathbf{e}_m,$$

where  $\mathbf{a}^m$  is given in (9). The expression for  $\mathbf{b}^m$  in (8) follows from the simplification

$$T_{\bar{q}}G \times T_{\bar{q}}\mathbf{e}_m = T_{\bar{q}}(G \times \mathbf{e}_m) = \bar{q} \cdot (G \times \mathbf{e}_m) \cdot q.$$

Theorem 3.2 is proved. □

### 3.3 Reconstruction algorithm for $(\sigma, q)$

#### 3.3.1 Evolving a unit quaternion along a curve

Our plan is to integrate the differential system (8) along curves, so we now explain how to numerically evolve a quaternionic variable along a curve  $\mathbf{x}(t) = (x_1(t), x_2(t), x_3(t))$ . For the time being, we denote  $q(t)$  such a function without reference to the curve used. Over such a curve, the evolution equation takes the form

$$\frac{dq}{dt} = \frac{1}{2} (q \cdot \mathbf{a}(q) + \mathbf{b} \cdot q), \quad (14)$$

with  $\mathbf{a} = \dot{x}_1 \mathbf{a}^1 + \dot{x}_2 \mathbf{a}^2 + \dot{x}_3 \mathbf{a}^3$  and each  $\mathbf{a}^m$  defined in (9), similarly for  $\mathbf{b} = \dot{x}_1 \mathbf{b}^1 + \dot{x}_2 \mathbf{b}^2 + \dot{x}_3 \mathbf{b}^3$  with each  $\mathbf{b}^m$  defined in (8).

Upon viewing  $q$  as a four-vector  $[q_0 \ q_1 \ q_2 \ q_3]^T$ ,  $\mathbf{a} = a_1\mathbf{e}_1 + a_2\mathbf{e}_2 + a_3\mathbf{e}_3$  and similarly for  $\mathbf{b}$ , (14) takes the form of the following matrix-vector multiplication

$$\frac{d}{dt} \begin{bmatrix} q_0 \\ q_1 \\ q_2 \\ q_3 \end{bmatrix} = \frac{1}{2} \left( \begin{bmatrix} 0 & -a_1 & -a_2 & -a_3 \\ a_1 & 0 & a_3 & -a_2 \\ a_2 & -a_3 & 0 & a_1 \\ a_3 & a_2 & -a_1 & 0 \end{bmatrix} + \begin{bmatrix} 0 & -b_1 & -b_2 & -b_3 \\ b_1 & 0 & -b_3 & b_2 \\ b_2 & b_3 & 0 & -b_1 \\ b_3 & -b_2 & b_1 & 0 \end{bmatrix} \right) \begin{bmatrix} q_0 \\ q_1 \\ q_2 \\ q_3 \end{bmatrix}, \quad (15)$$

or in short, letting  $Q = [q_0 \ q_1 \ q_2 \ q_3]^T$  and  $\Omega = A + B$  the sum of the  $4 \times 4$  matrices above,

$$\dot{Q}(t) = \frac{1}{2}\Omega(t, Q(t))Q(t) \quad \text{where} \quad \Omega(t, Q(t)) \quad \text{is skew-symmetric.}$$

This shows that this dynamical system has an obvious conserved quantity,

$$\frac{d}{dt} (Q^T Q) = \dot{Q}^T Q + Q^T \dot{Q} = Q^T \Omega^T Q + Q^T \Omega Q = 0,$$

by skew-symmetry of  $\Omega$ . Thus  $|q|^2 = Q^T Q \equiv 1$  for all time  $t$  at the continuous level. One way to enforce norm conservation numerically is to implement the scheme

$$Q(t+h) = \exp(h\Omega(t)/2)Q(t) = (1 + h\Omega(t)/2 + \dots)Q(t),$$

where, since  $\Omega(t)$  is skew-symmetric,  $\exp(h\Omega(t)/2)$  is norm-preserving. With the decomposition  $\Omega = A + B$  with  $A$  and  $B$  commuting, we find that

$$\exp(h\Omega/2) = \exp(hA/2) \exp(hB/2).$$

On to computing each exponential, we find that  $A^2 = -|\mathbf{a}|^2 I$  (with  $|\mathbf{a}|^2 = a_1^2 + a_2^2 + a_3^2$ ), and similarly,  $B^2 = -|\mathbf{b}|^2 I$ . This implies, for every natural  $p$ ,

$$A^{2p} = (-1)^p |\mathbf{a}|^{2p} I, \quad A^{2p+1} = (-1)^p |\mathbf{a}|^{2p} A,$$

similarly for  $B$ . Using this identity in the series of the exponential, we arrive at the final scheme

$$Q(t+h) = \exp(hA/2) \exp(hB/2) Q(t), \quad \text{where}$$

$$\exp\left(\frac{hA}{2}\right) = \cos\left(\frac{h|\mathbf{a}|}{2}\right) I + \sin\left(\frac{h|\mathbf{a}|}{2}\right) \frac{A}{|\mathbf{a}|}, \quad \exp\left(\frac{hB}{2}\right) = \cos\left(\frac{h|\mathbf{b}|}{2}\right) I + \sin\left(\frac{h|\mathbf{b}|}{2}\right) \frac{B}{|\mathbf{b}|}. \quad (16)$$

### 3.3.2 Algorithm summary

To evolve  $q$  along the curve (14), we do the following at each time-step:

- compute  $A$  via the formula (9) and  $B$  via (8).
- evolve  $q$  according to (16).

Once  $q$  is reconstructed along a family of curves covering the computational domain, one may reconstruct  $\sigma$  via (5), i.e.,

$$\nabla \log \sigma = \frac{1}{3} \nabla \log \det H + \frac{4}{3} (T_{\bar{q}} V_{ij}^s)_i T_{\bar{q}} \mathbf{e}_j,$$

or taking the dot product with  $\mathbf{e}_m$  and using that  $\langle T_{\bar{q}} \mathbf{e}_j, \mathbf{e}_m \rangle = \langle \mathbf{e}_j, T_{\bar{q}} \mathbf{e}_m \rangle = (T_{\bar{q}} \mathbf{e}_m)_j$  :

$$\partial_m \log \left( \frac{\sigma}{(\det H)^{\frac{1}{3}}} \right) = \frac{4}{3} (T_{\bar{q}} V_{ij}^s)_i (T_{\bar{q}} \mathbf{e}_m)_j, \quad m = 1, 2, 3. \quad (17)$$

Since the right-hand sides of these equations are completely known at this point, one may avoid using ODEs (whose outcome would depend on the choice of direction of propagation) by just solving an elliptic PDE. Numerically, what we do is compute

$$\sigma = (\det H)^{1/3} e^v,$$

where  $v$  is the unique solution to the Poisson problem

$$\Delta v = \frac{4}{3} \partial_m ((T_{\bar{q}} V_{ij}^s)_i (T_{\bar{q}} \mathbf{e}_m)_j) \quad (\text{in } X), \quad v|_{\partial X} = \log \left( \frac{\sigma}{(\det H)^{1/3}} \right) |_{\partial X}. \quad (18)$$

**Remark 3.3** (On the stability of the approach). *The stability of reconstructing  $q$  via integrating system (8) will be the same as that of the stability of reconstructing  $R$  via integration of (6), which was previously established in [29, Prop. 4.3.6]. Based on Gronwall's lemma, propagating errors along integration curves, one obtains a pointwise control of  $q$  in terms of the  $W^{1,\infty}$  Sobolev norm of the functionals  $H_{ij}$ . In turn, the right-hand side of (18) is controlled in  $H^{-1}$  norm by the  $W^{1,\infty}$  norm of the functionals  $H_{ij}$  and the reconstructed  $v$  (and thus  $\sigma$ ) will be controlled in  $H^1$  norm by the  $W^{1,\infty}$  norm of the functionals  $H_{ij}$ .*

## 4 Anisotropic reconstruction from 3 + 2 solutions and more

We now consider the reconstruction problem of a fully anisotropic tensor  $\gamma$ , which we write as  $\gamma = \tilde{\gamma} \tau$ , with  $\tilde{\gamma}$  the anisotropic structure satisfying  $\det \tilde{\gamma} = 1$ , and  $\tau$  the scalar factor. We follow, and adapt to three dimensions (using 3D vector identities rather than exterior algebra), the exposition in the article [32] for the reconstruction of  $\tilde{\gamma}$  followed by that of  $\tau$ .

Define  $\tilde{A} = \tilde{\gamma}^{\frac{1}{2}}$  the all-positive squareroot of  $\tilde{\gamma}$  and  $A$  the all-positive squareroot of  $\gamma$ . Suppose one starts from measurements  $H = \{H_{ij}\}_{1 \leq i, j \leq 3}$  associated with three solutions  $(u_1, u_2, u_3)$  whose gradients are linearly independent over an open set  $\Omega$ , and denote  $S_i = A \nabla u_i$  for  $1 \leq i \leq 3$  as well as  $S := [S_1 | S_2 | S_3]$ .

## 4.1 Preliminaries

### 4.1.1 Reconstruction of $\tilde{A}S$ from additional measurements

Call  $v$  an additional conductivity solution in addition to  $(u_1, u_2, u_3)$ . By the basis assumption,  $A \nabla v$  must decompose along  $S_1, S_2, S_3$ , via coefficients  $\mu_1, \mu_2, \mu_3$ , i.e.

$$A \nabla v + \sum_{i=1}^3 \mu_i S_i = 0. \quad (19)$$

An important observation is that the coefficient  $\mu_i$  are *known from the power densities* of the set of solutions  $(u_1, u_2, u_3, v)$ , as may readily be seen from taking the inner product of (19) with  $A \nabla u_1, A \nabla u_2, A \nabla u_3$ . A second crucial observation is the following:

**Lemma 4.1.** *Let  $u_1, u_2, u_3, v$  as above and  $\mu_1, \mu_2, \mu_3$  the coefficients in (19). Upon defining  $\mathbf{Z} := [\nabla \mu_1 | \nabla \mu_2 | \nabla \mu_3]$ , we have the following orthogonality relations*

$$0 = \mathbf{Z} : \tilde{A}S, \quad (20)$$

$$0 = \mathbf{Z}H\Omega_1 : \tilde{A}S = \mathbf{Z}H\Omega_2 : \tilde{A}S = \mathbf{Z}H\Omega_3 : \tilde{A}S, \quad (21)$$

where  $A : B := \text{tr}(A^T B)$  and

$$\Omega_i := \mathbf{e}_{i+1} \otimes \mathbf{e}_{i+2} - \mathbf{e}_{i+2} \otimes \mathbf{e}_{i+1}, \quad \text{for } i = 1, 2, 3 \text{ with } i+1, i+2 \text{ defined modulo } 3.$$

*Proof.* To derive (20), apply the operator  $\nabla \cdot (A \cdot)$  to (19), combining with the chain rule and using the conductivity equations, to obtain

$$0 = \sum_{i=1}^3 \langle \nabla \mu_i, AS_i \rangle = [\nabla \mu_1 | \nabla \mu_2 | \nabla \mu_3] : AS = [\nabla \mu_1 | \nabla \mu_2 | \nabla \mu_3] : \tilde{A}S.$$

To derive (21), we use that a gradient field is curl-free. Since we have  $\nabla \times \nabla v = 0$ , if we apply  $A^{-1}$  to (19) followed by the curl operator  $\nabla \times$  (and using that  $\nabla \times (fV) = \nabla f \times V + f \nabla \times V$  for  $f$  a function and  $V$  a vector field), we arrive at

$$\nabla \mu_1 \times \tilde{A}^{-1}S_1 + \nabla \mu_2 \times \tilde{A}^{-1}S_2 + \nabla \mu_3 \times \tilde{A}^{-1}S_3 = 0. \quad (22)$$

Using the identity

$$\langle A \times (B \times C), D \rangle = \langle A, C \rangle \langle B, D \rangle - \langle A, B \rangle \langle C, D \rangle,$$

we can then derive, for  $(p, q) \in \{(1, 2), (2, 3), (3, 1)\}$ ,

$$0 = \left\langle \tilde{A}S_p \times (\nabla\mu_i \times \tilde{A}^{-1}S_i), \tilde{A}S_q \right\rangle = H_{pi} \left\langle \nabla\mu_i, \tilde{A}S_q \right\rangle - H_{qi} \left\langle \nabla\mu_i, \tilde{A}S_p \right\rangle.$$

If we define  $\mathbf{C} = [C_1|C_2|C_3] := [\nabla\mu_1|\nabla\mu_2|\nabla\mu_3]H = \mathbf{Z}H$ , known from data, then the equations above can be recast as three additional orthogonality conditions

$$[-C_2|C_1|0] : \tilde{A}S = [0|-C_3|C_2] : \tilde{A}S = [-C_3|0|C_1] : \tilde{A}S = 0.$$

For  $i = 1, 2, 3$ , define  $\Omega_i := \mathbf{e}_{i+1} \otimes \mathbf{e}_{i+2} - \mathbf{e}_{i+2} \otimes \mathbf{e}_{i+1}$ , where  $i + 1$  and  $i + 2$  are defined modulo 3. Then the three conditions above can be recasted as

$$\mathbf{Z}H\Omega_1 : \tilde{A}S = \mathbf{Z}H\Omega_2 : \tilde{A}S = \mathbf{Z}H\Omega_3 : \tilde{A}S = 0.$$

Lemma 4.1 is proved.  $\square$

In short, one additional solution  $v$ , via its power densities with the initial basis, provides 4 orthogonality constraints on the matrix  $\tilde{A}S$ . Let now  $v_1, v_2$  be two additional solutions, with matrices  $\mathbf{Z}_1, \mathbf{Z}_2$  as defined in Lemma 4.1, and suppose the following hypothesis:

**Hypothesis 4.2** (3+2 ( $X'$ )). *Let  $X' \subset X$  open. Suppose  $(u_1, u_2, u_3, v_1, v_2)$  are five solutions of (1), such that, at every point  $\mathbf{x} \in X'$*

(i)  $\nabla u_1(\mathbf{x}), \nabla u_2(\mathbf{x}), \nabla u_3(\mathbf{x})$  are linearly independent.

(ii) With  $\mathbf{Z}_1, \mathbf{Z}_2$  defined above, the eight matrices below are linearly independent:

$$\mathbf{Z}_j(\mathbf{x}), \mathbf{Z}_j(\mathbf{x})H(\mathbf{x})\Omega_1, \mathbf{Z}_j(\mathbf{x})H(\mathbf{x})\Omega_2, \mathbf{Z}_j(\mathbf{x})H(\mathbf{x})\Omega_3, \quad j = 1, 2,$$

Under Hypothesis 4.2, the additional solutions  $v_1, v_2$  generate 8 non-redundant orthogonality conditions on  $\tilde{A}S$ , so that the matrix  $\tilde{A}S$  is determined up to a scalar factor, which in turn is determined using the normalization condition

$$\det(\tilde{A}S) = \sqrt{\det H}.$$

#### 4.1.2 Reconstruction of $\tilde{\gamma}$ from $\tilde{A}S$

Once  $\tilde{A}S$  is reconstructed, one may reconstruct  $\tilde{\gamma}$  from the following observation: from the relation  $S^T S = H$ , we have  $Id = S^{-T} H S^{-1}$ , which in turn yields  $Id = S H^{-1} S^T$  upon taking inverses. The following identity then allows us to get  $\tilde{\gamma}$  out of  $\tilde{A}S$  and the matrix  $H$ :

$$\tilde{\gamma} = \tilde{A}\tilde{A}^T = \tilde{A}S H^{-1} S^T \tilde{A}^T = \tilde{A}S H^{-1} (\tilde{A}S)^T. \quad (23)$$

### 4.1.3 Subsequent reconstruction of $\tau$

We now provide equations which will set the stage for the algorithms of the next sections, reconstructing  $\tau$  after  $\tilde{A}S$  and  $\tilde{\gamma}$  have been reconstructed. They are given by the following:

**Lemma 4.3.** *Suppose  $u_1, u_2, u_3$  have linearly independent gradients over  $X' \subset X$ , let  $H = \{H_{ij}\}_{1 \leq i, j \leq 3}$  their power densities. Denote  $H^{pq} := (H^{-1})_{pq}$ , and  $\tilde{H}_{pq}$  the cofactor  $(p, q)$  of the matrix  $H$  (so that  $\tilde{H}_{pq} = |H|H^{pq}$ ). Under knowledge of  $\tilde{\gamma}$ , the following equations hold:*

$$\nabla \log \tau = \frac{2}{3}|H|^{-\frac{1}{2}} \left\langle \nabla \left( |H|^{\frac{1}{2}} H^{jl} \right), \tilde{A}S_l \right\rangle \tilde{A}^{-1}S_j = \frac{1}{3} \nabla \log |H| + \frac{2}{3} \left\langle \nabla H^{jl}, \tilde{A}S_l \right\rangle \tilde{A}^{-1}S_j, \quad (24)$$

$$\nabla \log \tau = \frac{1}{3} \nabla \log |H| + \frac{2}{3} \tilde{\gamma}^{-1} \left\langle \nabla H^{jl}, \tilde{A}S_l \right\rangle \tilde{A}S_j. \quad (25)$$

$$|H| \tilde{\gamma} \nabla \log \tau = \frac{2}{3} \left\langle \nabla \tilde{H}_{jl}, \tilde{A}S_l \right\rangle \tilde{A}S_j - \frac{1}{3} \tilde{\gamma} \nabla |H|. \quad (26)$$

*Proof.* Equation (24) is nothing but [32, Eq. (7)] adapted to three dimensions and (25) comes immediately from using that  $\tilde{A}^{-1} = \tilde{\gamma}^{-1} \tilde{A}$ . To derive (26), let us modify (24) as follows:

$$\begin{aligned} \nabla \log \tau &= \frac{2}{3} |H|^{-\frac{1}{2}} \left\langle \nabla \left( |H|^{-\frac{1}{2}} \tilde{H}_{jl} \right), \tilde{A}S_l \right\rangle \tilde{A}^{-1}S_j \\ &= \frac{2}{3} |H|^{-1} \left\langle \nabla \tilde{H}_{jl}, \tilde{A}S_l \right\rangle \tilde{A}^{-1}S_j + \frac{2}{3} |H|^{\frac{1}{2}} H^{jl} \left\langle \nabla |H|^{-\frac{1}{2}}, \tilde{A}S_l \right\rangle \tilde{A}^{-1}S_j \\ &= \frac{2}{3} |H|^{-1} \left\langle \nabla \tilde{H}_{jl}, \tilde{A}S_l \right\rangle \tilde{A}^{-1}S_j + \frac{2}{3} |H|^{\frac{1}{2}} \nabla |H|^{-\frac{1}{2}} \\ &= \frac{2}{3} |H|^{-1} \left\langle \nabla \tilde{H}_{jl}, \tilde{A}S_l \right\rangle \tilde{A}^{-1}S_j - \frac{1}{3} \nabla \log |H| \end{aligned}$$

Multiplying by  $|H| \tilde{\gamma}$  and using that  $\tilde{\gamma} \tilde{A}^{-1} = \tilde{A}$ , we obtain (26).  $\square$

Equations (24) or (25) are to be used over some set  $X'$  where Hypothesis 4.2 is satisfied. In particular, when it is satisfied globally over  $X$ , they will make the basis of the **3+2 algorithm** presented in Section 4.2.

On the other hand, when  $\det H$  vanishes and Hypothesis 4.2 cannot be satisfied throughout  $X$ , such equations become singular on the zero set of  $\det H = |H|$ , since then the terms  $H^{jl}$ , containing negative powers of  $|H|$ , become singular. Then one may use (26) instead, as the latter equation becomes zero at those points where  $\det H$  may vanish, but remains bounded otherwise. Combining such equations associated with more than one basis of solutions will be the basis of the **stabilized 3+2 algorithm**, presented Section 4.3, allowing for a global reconstruction of  $\gamma$  even when Hypothesis 4.2 cannot be satisfied throughout  $X$ .

## 4.2 The 3 + 2 algorithm

Based on the considerations above, we first formulate a so-called 3 + 2 reconstruction algorithm. Here and below,  $(u_1, u_2, u_3, v_1, v_3)$  are assumed to satisfy Hypothesis 4.2 globally over  $X$ .

**A. Reconstruction of  $\tilde{A}S$ .** 1. Compute the power densities of  $(v_1, v_2)$  with the initial basis:

$$H_{41}, H_{42}, H_{43}, H_{51}, H_{52}, H_{53}.$$

2. Out of these power densities and the matrix  $H = \{H_{ij}\}_{1 \leq i, j \leq 3}$ , compute the coefficients  $\mu_1^{(1)}, \mu_2^{(1)}, \mu_3^{(1)}$  and  $\mu_1^{(2)}, \mu_2^{(2)}, \mu_3^{(2)}$ , solutions of the systems:

$$H \begin{bmatrix} \mu_1^{(1)} \\ \mu_2^{(1)} \\ \mu_3^{(1)} \end{bmatrix} = - \begin{bmatrix} H_{41} \\ H_{42} \\ H_{43} \end{bmatrix}, \quad H \begin{bmatrix} \mu_1^{(2)} \\ \mu_2^{(2)} \\ \mu_3^{(2)} \end{bmatrix} = - \begin{bmatrix} H_{51} \\ H_{52} \\ H_{53} \end{bmatrix}. \quad (27)$$

3. Compute the eight matrices

$$\mathbf{Z}_j = [\nabla \mu_1^{(j)} | \nabla \mu_2^{(j)} | \nabla \mu_3^{(j)}], \quad \mathbf{Z}_j H \Omega_1, \quad \mathbf{Z}_j H \Omega_2, \quad \mathbf{Z}_j H \Omega_3, \quad j = 1, 2. \quad (28)$$

4. Compute a matrix which is perpendicular to the eight matrices above, call it  $B$ , and normalize it as

$$B \leftarrow \left( \frac{\sqrt{\det H}}{\det B} \right)^{\frac{1}{3}} B,$$

where we extend the definition  $x^{\frac{1}{3}} = -|x|^{\frac{1}{3}}$  if  $x$  is negative, so that  $\det B = \sqrt{\det H}$  and  $B$  should be an approximation of  $\tilde{A}S$ .

To compute  $B$ , one may use a standard numerical algorithm such as the singular value decomposition (SVD) for the  $9 \times 8$  matrix whose 8 columns are the vectorization of the matrices (28).<sup>2</sup>

**B. Reconstruction of  $\tilde{\gamma}$  from  $\tilde{A}S$ .** With  $B$  as above, equation (23) suggests that an approximation  $G$  of  $\tilde{\gamma}$  be obtained via the pointwise formula  $G = BH^{-1}B^T$ .

**C. Reconstruction of  $\tau$  from  $\tilde{A}S$  and  $\tilde{\gamma}$ .** With  $B$  and  $G$  as above, and denoting  $B_i$  the  $i$ -th column of  $B$ , equation (25) suggests that  $\tau$  can be reconstructed via the equation:

$$\nabla \log \tau = \frac{1}{3} \nabla \log |H| + \frac{2}{3} \left\langle \nabla H^{jl}, B_l \right\rangle G^{-1} B_j. \quad (29)$$

<sup>2</sup>For example, in Matlab this is done by the commands  $[U, \mathbf{s}, V] = \text{svd}(A)$ , if columns of  $A$  are vectorization of the matrices (28). Then  $B$  can be set as the last column of  $U$ , i.e.,  $U(:, 9)$ .

As the right-hand-side is completely known and  $\log \tau$  is assumed to be known at the boundary, one may take the divergence of the equation above and solve a Poisson equation for  $\log \tau$  with known Dirichlet boundary condition. (This is another advantage of this method over an ODE-based approach as in Section 3, if more than 3 solutions are being considered for inversion purposes.)

### 4.3 The stabilized algorithm

The 3+2 algorithm above works only if Hypothesis 4.2 is satisfied throughout  $X$ . Wherever this fails to be so, the matrices  $H$  and  $S$  become singular. While we observe that they tend to do so on sets of codimension 1, such singularities prevent a successful reconstruction in the vicinity of these regions. A way to cope with this source of instability is to use more than 2, say  $m$ , “3+2” sets, each of which satisfies Hypothesis 4.2 over some  $X_k \subset X$  and such that the  $X_k$ ’s cover  $X$ .

**Hypothesis 4.4** ( $m(3+2)$ ). *Suppose  $X_1, \dots, X_m$  is an open cover of  $X$  and for each  $1 \leq k \leq m$ , there exists  $(u_1^{(k)}, u_2^{(k)}, u_3^{(k)}, v_1^{(k)}, v_2^{(k)})$  satisfying Hypothesis 4.2 over  $X_k$ .*

Hypothesis 4.4 allows us to combine  $m$  3+2 algorithms into a globally stable algorithm.

**Remark 4.5.** *As Section 5.5 shows, some solutions can be used more than once so that the number of solutions required does not necessarily grow linearly with  $m$ .*

We now describe how to modify steps **A**, **B**, **C** above so that they are stable even when certain determinants vanish.

**A’. Stabilized reconstruction of  $\tilde{A}S$  up to a constant.** In step **A**, the orthogonality conditions do not change if multiplied by a scalar function, the only exception being that they become vacuous when that function vanishes. This is the tradeoff we pay to avoid instabilities. In order to never divide by small quantities for the sake of stability, we propose the following. In step **A.2**, the  $\mu_i^{(j)}$  can be written as  $\frac{\tilde{\mu}_i^{(j)}}{|H|}$  and the  $\tilde{\mu}_i^{(j)}$ ’s is the matrix of cofactors of  $H$  multiplied by the vector in the right-hand-side. The matrix  $\mathbf{Z}_j$  can be replaced by the matrix  $|H|^2 \mathbf{Z}_j$ , whose columns are given by

$$\mathbf{Z}'_j := |H|^2 \mathbf{Z}_j = [ |H| \nabla \tilde{\mu}_1^{(j)} - \tilde{\mu}_1^{(j)} \nabla |H|, |H| \nabla \tilde{\mu}_2^{(j)} - \tilde{\mu}_2^{(j)} \nabla |H|, |H| \nabla \tilde{\mu}_3^{(j)} - \tilde{\mu}_3^{(j)} \nabla |H| ]. \quad (30)$$

Such a matrix still gives rise to the four matrices which are orthogonal to  $\tilde{A}S$ , but where we never divide by a small quantity. Therefore, a first change to the algorithm is simply to compute the matrix  $\mathbf{Z}'_j$  defined in (30) instead of  $\mathbf{Z}_j$ , and do everything else as usual. Now let  $B'$  a matrix orthogonal to

$$\mathbf{Z}'_j, \quad \mathbf{Z}'_j H \Omega_1, \quad \mathbf{Z}'_j H \Omega_2, \quad \mathbf{Z}'_j H \Omega_3, \quad j = 1, 2,$$

which we do not normalize for stability purposes. All we know is that  $B'$  is proportional to  $\tilde{A}S$  almost everywhere, a relation which we denote  $B' = b\tilde{A}S$ .

**B'. Stabilized reconstruction of  $\tilde{\gamma}$  up to a constant.** In step **B**, the instability may arise from the fact that when  $|H|$  becomes small, computation of  $H^{-1}$  becomes unstable. We may then replace  $H^{-1}$  by the cofactor matrix  $\tilde{H}$ . That is, with  $B'$  as above,  $G' = B'\tilde{H}(B')^T$  should be almost everywhere proportional to  $\tilde{\gamma}$ . If we denote this relation  $G' = g\tilde{\gamma}$ , then we can determine  $g$  in terms of  $b$  by taking determinants:

$$g^3 = \det G' = (\det B')^2 \det \tilde{H} = (b^3 |H|^{\frac{1}{2}})^2 |H|^2 \implies g = b^2 |H|. \quad (31)$$

**C'.** With  $B'$  and  $G'$  as above, and given the relation (31), equation (26) can be written in terms of the matrices  $B'$  and  $G'$  as follows:

$$|H|G'\nabla \log \tau = \frac{2}{3}|H|\left\langle \nabla \tilde{H}_{jl}, B'_l \right\rangle B'_j - \frac{1}{3}G'\nabla |H|. \quad (32)$$

Such an equation recovers  $\nabla \log \tau$  almost everywhere and is identically zero otherwise.

Bearing in mind the modified steps **A'**, **B'**, **C'** associated with a single basis of solutions, we now explain how to combine such algorithms using multiple bases.

**Outline of the stabilized algorithm.** Assume Hypothesis 4.4 holds for some  $m \geq 2$ .

- Let  $H^{(1)}, \dots, H^{(m)}$  be the  $3 \times 3$  matrices of power densities associated with  $m$  bases. Since Hypothesis 4.4 holds, we have that  $\sum_{j=1}^m |H^{(j)}|$  is nowhere vanishing (even if either determinant can vanish at times).
- Compute two additional solutions. For either basis and with these two additional solutions, run steps **A'** and **B'** described above to obtain  $\{B'^{(j)}\}_{j=1}^m, \{G'^{(j)}\}_{j=1}^m$ , approximations (up to multiplicative constants) of  $\{\tilde{A}S^{(j)}\}_{j=1}^m$  and  $\tilde{\gamma}$ , respectively.
- Summing the equations (32) obtained for each basis, the matrix

$$M := |H^{(1)}|G'^{(1)} + \dots + |H^{(m)}|G'^{(m)}$$

should be globally invertible by assumption, and  $\nabla \log \tau$  and the anisotropic structure  $\tilde{\gamma}$  can be globally recovered from the equations

$$\begin{aligned} \nabla \log \tau &= M^{-1} \sum_{k=1}^m \left( \frac{2}{3}|H^{(k)}|\left\langle \nabla \tilde{H}_{jl}^{(k)}, B'_l{}^{(k)} \right\rangle B'_j{}^{(k)} - \frac{1}{3}G'^{(k)}\nabla |H^{(k)}| \right), \\ \tilde{\gamma} &= (\det M)^{-1/3}M. \end{aligned} \quad (33)$$

As usual, since the right-hand-side of the equation for  $\log \tau$  is completely known, one may take a divergence and solve a Poisson problem, assuming  $\tau$  known at the boundary.

## 5 Numerical experiments

In this section, we will provide numerical illustrations of the algorithms presented above. Three experiments will be performed, in which the conductivity  $\gamma$  in (1) will be different versions of a pair of interlocked tori, which we define in Section 5.1 below. We will denote the three conductivities corresponding to each of the examples by  $\gamma_1, \gamma_2$  and  $\gamma_3$ . The three reconstructions will be of increasing difficulty and will serve to illustrate the key points of the algorithms detailed in Sections 3 and 4. The MATLAB implementation of the following experiments are publicly available in an online repository [33].

**Exp1 (Section 5.3):** Reconstruction of a scalar conductivity  $\gamma_1$  using power densities associated with three solutions, via solving a dynamical system as described in Section 3.

**Exp2 (Section 5.4):** Reconstruction of an anisotropic perturbation of the identity tensor  $\gamma_2$  from  $3 + 2$  solutions, following the approach described in Section 4.2.

**Exp3 (Section 5.5):** Reconstruction of an anisotropic conductivity tensor  $\gamma_3$  that is similar to  $\gamma_2$  in form, but whose anisotropic perturbation has high enough amplitude so that Hypothesis 4.2 is violated. We will perform the reconstruction using more than  $3 + 2$  solutions, following the approach described in Section 4.3.

### 5.1 Interlocked tori

In this section, we define the conductivities  $\gamma_1, \gamma_2$  and  $\gamma_3$  to be used for numerical experiments below. They will be the identity  $Id$  plus a tensor whose level set will be two interlocked tori like those shown on the right plot in Fig.1. Our experiments we will be conducted in the cubic domain,  $X = (-1, 1)^3$ .

Let us describe a torus  $T$  by the quadruple  $T = (c, \phi, R, r)$ , see Fig.1 (left). The torus will be centered at  $c \in \mathbb{R}^3$ , oriented by a unit vector  $\phi \in \mathbb{R}^3$  orthogonal to the plane containing the generating circle, and have a radii of  $r$  and  $R$  for the small and great circles, respectively. Given a torus  $T$ , let  $\chi_T$  be a smooth Gaussian kernel as a function of the distance to the generating circle. That is,  $\chi_T$  will have intensity one on the circle and will decay exponentially with respect to the distance to that circle.

$$\chi_T(\mathbf{x}) := \exp\left(-\frac{|\mathbf{x} - P(\mathbf{x})|^2}{2r^2}\right), \quad (34)$$

where  $P(\mathbf{x})$  maps  $\mathbf{x}$  to the its closest point on the generating circle of  $T$ ,

$$P(\mathbf{x}) := c + R \frac{\mathbf{x} - c - \langle \mathbf{x} - c, \phi \rangle \phi}{|\mathbf{x} - c - \langle \mathbf{x} - c, \phi \rangle \phi|}. \quad (35)$$

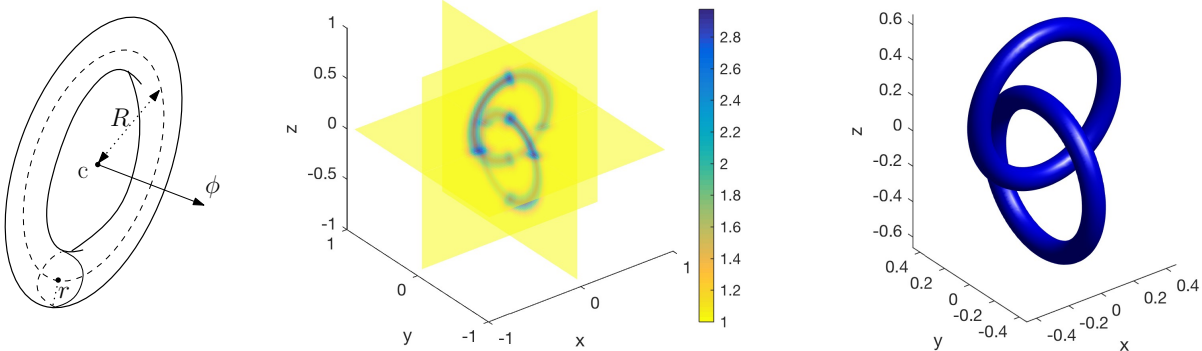


Figure 1: Parametrization of a torus (left), 3D slice plot of scalar interlocked tori  $\gamma_1$  (36) (middle), and its isosurface  $\{x : \gamma_1(x) = 1.8\}$  (right)

Then we define  $\gamma_T$  to be a smooth symmetric tensor of rank one, whose range belongs in the tangents of the generating circle of  $T$ , whose amplitude will be adjusted by  $\chi_T$ ,

$$\gamma_T(x) := \chi_T(x)(\widehat{x}_c \times \phi) \otimes (\widehat{x}_c \times \phi), \quad \text{where} \quad \widehat{x}_c := \frac{x - c}{|x - c|}.$$

For each of our experiments, we will use two interlocked tori, one centered in the upper-half cube  $\{z > 0\}$  (denoted by  $T_u$ ), another centered in the lower-half cube  $\{z < 0\}$  (denoted by  $T_d$ ). But we will vary the precise centers and radii.

Let the tori  $T_{u1}$ ,  $T_{d1}$ ,  $T_{u2}$  and  $T_{d2}$  given by

$$T_{u1} = (c_1, \phi_1, R_1, r_1) \quad \text{and} \quad T_{d1} = (-c_1, \phi_2, R_1, r_1) \quad \text{where} \quad \begin{cases} c_1 = (0, 0, 0.2), \\ \phi_1 = (1, 0, 0), \\ \phi_2 = (0, 1, 0), \\ R_1 = 0.4, \\ r_1 = 0.1, \end{cases}$$

$$T_{u2} = (c_2, \phi_1, R_2, r_2) \quad \text{and} \quad T_{d2} = (-c_2, \phi_2, R_2, r_2) \quad \text{where} \quad \begin{cases} c_2 = (0, 0, 0.5), \\ R_2 = 0.8, \\ r_2 = 0.1, \end{cases}$$

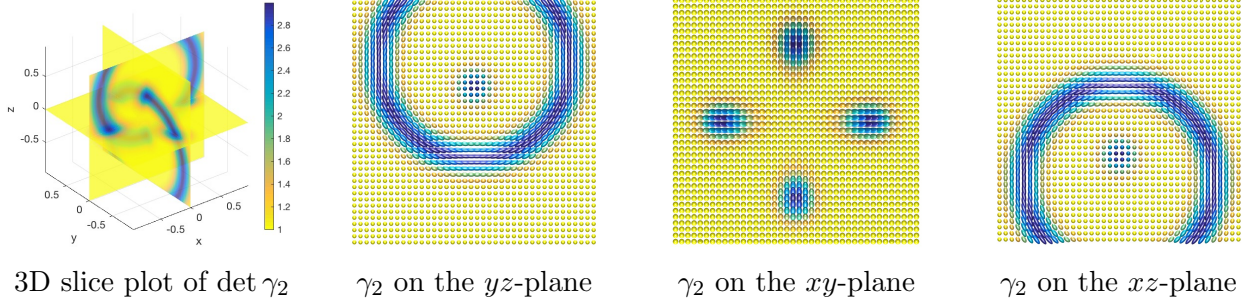


Figure 2: Anisotropic interlocked tori  $\gamma_2$  (37) of amplitude  $k_2 = 2$ . The axes of the ellipsoids represent the anisotropy at each spatial point [16].

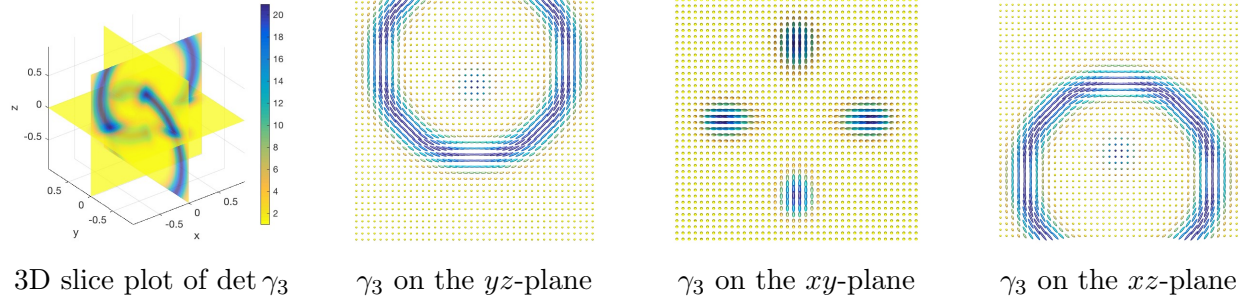


Figure 3: Anisotropic interlocked tori  $\gamma_3$  (38) of amplitude  $k_3 = 20$ . The axes of the ellipsoids represent the anisotropy at each spatial point [16].

We then define the conductivities  $\gamma_1, \gamma_2$  and  $\gamma_3$  as follows,

$$\gamma_1 = 1 + k_1\chi_{T_{u_1}} + k_1\chi_{T_{d_1}} \quad \text{with } k_1 = 2, \quad (36)$$

$$\gamma_2 = Id + k_2\gamma_{T_{u_2}} + k_2\gamma_{T_{d_2}} \quad \text{with } k_2 = 2, \quad (37)$$

$$\gamma_3 = Id + k_3\gamma_{T_{u_2}} + k_3\gamma_{T_{d_2}} \quad \text{with } k_3 = 20. \quad (38)$$

Note that  $\gamma_1$  is a scalar corresponding to an isotropic case, whereas  $\gamma_2$  and  $\gamma_3$  are anisotropic. We plot the 3D slice plot of the scalar tori  $\gamma_1$  along with an isosurface in Fig.1. The 3D slice plot of  $\det \gamma$  as well as the representation of the anisotropy for each of the slices for  $\gamma_1$  and  $\gamma_2$  are given on Fig.2 and Fig.3, respectively. For this representation, we use the code developed in [16], where 3D ellipsoids are used to represent symmetric positive definite matrices; the principal axes correspond to the eigenvectors, and the widths along them correspond to the eigenvalues.

Our choice of conductivities is justified as follows. As is now well-known, certain conductivities  $\gamma$  are such that  $\gamma$ -harmonic extensions of global diffeomorphism of the boundary fail to make global diffeomorphism of the interior of the domain for dimension three (unlike in two).

A famous example appears in [19], presented in the context of periodic structures. This was elaborated upon for a domain with boundary in [6]. The main idea therein is that for scalar interlocked tori with high conductivity (e.g.,  $\gamma = 1 + k\chi_{T_1} + k\chi_{T_2}$  with  $k$  large), conduction of values along highly conductive regions creates topological changes in the isosurfaces of the solutions, which result in regions where three given solutions have linearly dependent gradients.

For our purposes in demonstrating the efficiency of our approach, we exacerbate these topological changes even more, by using the anisotropic tensor  $\gamma_3$  defined in (38) whose diffusion is especially high along the generating circles of the two tori.

## 5.2 Numerical implementation

The forward problem for the three experiments that appear in Sections 5.3, 5.4, and 5.5 are solved using the finite element method [18]: the solutions to the conductivity problems are computed using piecewise quadratic elements on an unstructured tetrahedral mesh with maximal diameter  $h_{\max} = 0.05$ . The power densities  $\{H_{ij}\}$  are computed by first evaluating the finite element solutions and their gradients for uniform Cartesian grid-points, then computing the inner-product point-wise. The uniform grid of size  $128 \times 128 \times 128$  was used.

Once the power densities are generated as above, various reconstruction procedures outlined in Sections 3 and 4, are performed solely on the uniform Cartesian grid. For example, these procedures include the computation of the dynamical system (8) for quaternions, and the solution of the Poisson problems that follow from (18), (29), and (33) are solved on the uniform grid using the finite difference method [28]. Gradient computations necessary for preparing these systems are also computed using second-order finite differences.

## 5.3 Isotropic reconstructions via dynamical system

**Experiment 1.** Here we reconstruct the scalar interlocked tori  $\gamma_1$  (36) from the power densities  $H_{ij}(\mathbf{x})$  ( $i, j = 1, 2, 3$ ) of three solutions

$$u_1(\mathbf{x}), \quad u_2(\mathbf{x}), \quad u_3(\mathbf{x}), \quad (39)$$

which satisfy the boundary conditions

$$u_1(\mathbf{x})|_{\partial X} = x, \quad u_2(\mathbf{x})|_{\partial X} = y, \quad u_3(\mathbf{x})|_{\partial X} = z. \quad (40)$$

The determinant of the gradients of the solutions, i.e.  $\det(\nabla u_1, \nabla u_2, \nabla u_3)$ , does not vanish for this set of solutions, as shown in Fig.4.

We proceed to use the algorithm proposed in Section 3 to reconstruct  $\gamma_1$ . The dynamical system (8) for quaternions is solved along the straight line in the direction of the  $x$ -axis, along a Cartesian grid. The computed quaternionic system allows the reconstruction of the  $SO(3)$ -valued function arising from the local gradient system (6). We denote this function by  $R = (R_1, R_2, R_3)$

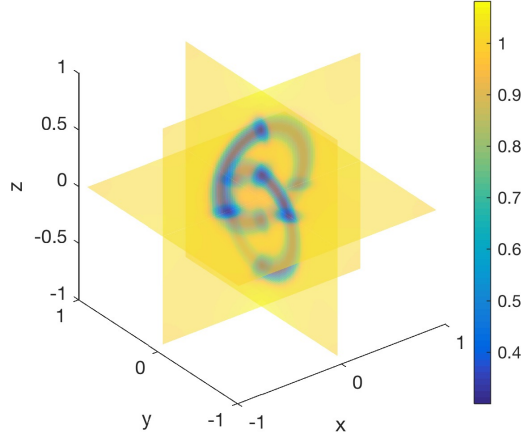


Figure 4: Exp. 1:  $\det(\nabla u_1, \nabla u_2, \nabla u_3)$  for three solutions (39, 40) obtained for the smooth scalar conductivity  $\gamma_1$  (36). Computed minimum: 0.3000.

	$\gamma_1$
Rel. $L^1$ error	0.00127075
Rel. $L^2$ error	0.00659273
Rel. $L^\infty$ error	0.05968462
Max. pointwise rel. error	0.06503202

Table 1: Exp. 1: Summary of reconstruction error for  $\gamma_1$  (36).

where  $R_i$  is the  $i$ -th basis vector after applying the rotation matrix to the canonical basis. The true  $R$  and the reconstruction error  $R$  are visualized in and Fig.5, respectively. In the relative error, one can clearly see the direction-dependence of the reconstruction, as the errors accumulate as the dynamical system is being integrated from the boundary at  $x = -1$ .

Finally, we reconstruct  $\gamma_1$  by solving the Poisson's problem (18). The reconstruction, along with its corresponding relative error are plotted in Fig.6. The error is concentrated near the region of high conductivity at the generating circle of the two tori. The reconstruction errors are summarized in Table 1. The relative  $L^1$  error is at 0.1% and pointwise relative error is less than 6%.

#### 5.4 Anisotropic reconstructions using 3 + 2 solutions

**Experiment 2.** We first demonstrate the success of the approach in a perturbative case where the unknown tensor  $\gamma_2$  (37) is close enough to a known  $\gamma_0$ , for which some background solutions

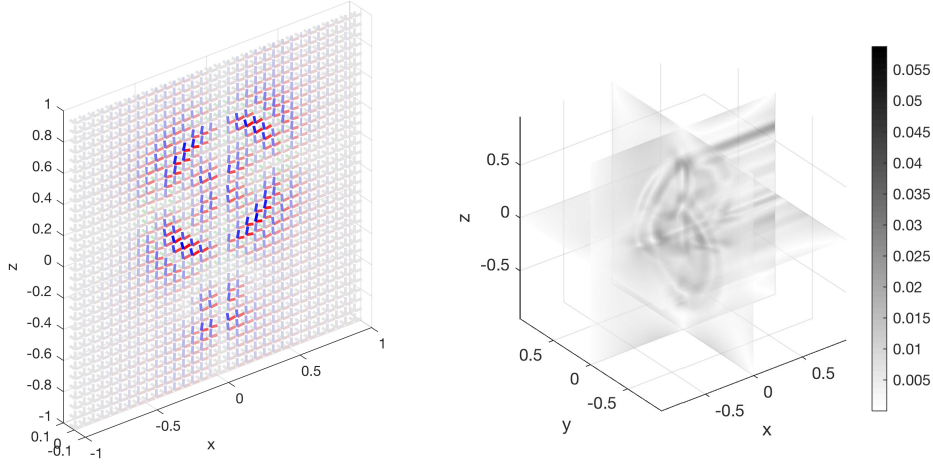


Figure 5: Exp. 1: True  $R$ , visualized by showing three components of the rotated standard basis ( $\mathbf{e}_1, \mathbf{e}_2, \mathbf{e}_3$ ) under the action of  $R$ , color-coded by red, green and blue, respectively (left). The strength of the colors indicate deviation from the identity measured in Frobenius norm. 3D slice plot of the relative reconstruction error, also measured in the Frobenius norm (right).

$(u_1, u_2, u_3, v_1, v_2)$  are known to fulfill the maximality conditions globally, that is,  $(\nabla u_1, \nabla u_2, \nabla u_3)$  forms a basis throughout  $X$ . By continuity of solutions with respect to the conductivity, generating power densities using the traces of the background solutions will provide functionals which still satisfy the maximality conditions globally, so the proposed algorithm should recover  $\gamma_2$  successfully.

Namely, let  $\gamma_0 = Id$  the identity tensor, and let the background conductivity solutions  $(u_1, u_2, u_3, v_1, v_2)$  be given by

$$u_1 = x, \quad u_2 = y, \quad u_3 = z, \quad v_1 = (x + 2)(y + 2), \quad v_2 = (x + 2)(z + 2).$$

For such solutions, we can compute directly that  $\det(\nabla u_1, \nabla u_2, \nabla u_3) = 1$  everywhere, and that the eight matrices defined in (28) are constant and equal to

$$\begin{aligned} \mathbf{Z}_1 &= \mathbf{e}_1 \otimes \mathbf{e}_2 + \mathbf{e}_2 \otimes \mathbf{e}_1, & \mathbf{Z}_1 H\Omega_1 &= \mathbf{e}_1 \otimes \mathbf{e}_3, & \mathbf{Z}_1 H\Omega_2 &= -\mathbf{e}_2 \otimes \mathbf{e}_3, & \mathbf{Z}_1 H\Omega_3 &= \mathbf{e}_2 \otimes \mathbf{e}_2 - \mathbf{e}_1 \otimes \mathbf{e}_1, \\ \mathbf{Z}_2 &= \mathbf{e}_1 \otimes \mathbf{e}_3 + \mathbf{e}_3 \otimes \mathbf{e}_1, & \mathbf{Z}_2 H\Omega_1 &= -\mathbf{e}_1 \otimes \mathbf{e}_2, & \mathbf{Z}_2 H\Omega_2 &= \mathbf{e}_1 \otimes \mathbf{e}_1 - \mathbf{e}_3 \otimes \mathbf{e}_3, & \mathbf{Z}_2 H\Omega_3 &= \mathbf{e}_3 \otimes \mathbf{e}_2. \end{aligned}$$

Therefore these matrices span  $\{Id\}^\perp \subset M_3(\mathbb{R})$  at every point. Then by a perturbation argument, for  $\gamma_2$  close enough to  $Id$ , the solutions of the problem  $\nabla \cdot (\gamma_2 \nabla u) = 0$  with  $u|_{\partial X}$  successively equal to the traces of  $(u_1, u_2, u_3, v_1, v_2)$ , still satisfy the conditions of Hypothesis 4.2 globally, setting the stage for a successful reconstruction.

First, we check numerically that the determinant of the gradients  $\det(\nabla u_1, \nabla u_2, \nabla u_3)$  do not vanish. We plot the determinant to the left in Fig.7, which reveals that the determinant

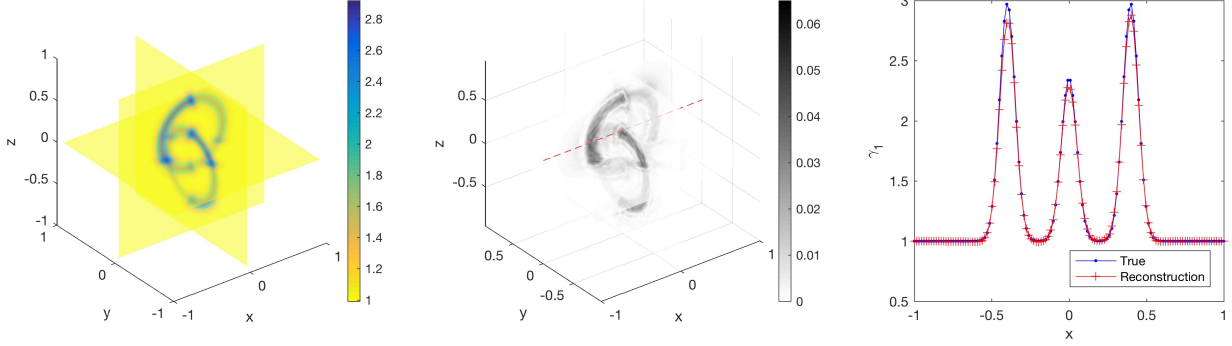


Figure 6: Exp. 1: 3D slice plot of the reconstruction of smooth scalar interlocked tori  $\gamma_1$  (36) (left) (to be compared with Fig.1, middle), the relative pointwise error (middle), and 1D comparison plot for  $\gamma_1$  and its reconstruction, along the line parallel to the  $x$ -axis through  $(y, z) = (0, 0.25)$  (right). The line is indicated by the red dashed line in the middle plot.

	$\tilde{\gamma}_2$	$\tau_2$	$\gamma_2$
Rel. $L^1$ error	0.00375946	0.00030364	0.00407776
Rel. $L^2$ error	0.00789942	0.00091769	0.00909787
Rel. $L^\infty$ error	0.11603989	0.01264201	0.12900887
Max. pointwise rel. error	0.16959084	0.01248439	0.15545096

Table 2: Exp. 2: Summary of reconstruction error for  $\gamma_2$  (37). The error for the tensor-valued functions computed pointwise by the Frobenius norm.

stays away from zero. Then we reconstruct the anisotropic tensor  $\tilde{\gamma}_2$  using the 3+2 algorithm outlined in Section 4.2. The reconstruction error is shown in Fig.7 (right).

Using the reconstructed  $\tilde{\gamma}_2$  we solve the Poisson problem (29), to obtain the scaling  $\tau_2$ . The reconstructed  $\tau_2$  and its relative error is shown in Fig.8. Finally, the error for the reconstructed  $\gamma_2$  itself is shown to the right in the same figure. The reconstruction errors are summarized in Table 2. The relative  $L^1$  error is at 0.4% and pointwise relative error is less than 15%. The volume of the domain that incurs pointwise relative error larger than 10% is 0.005%, hence the error is highly localized.

The error for the anisotropic part mostly originates from the approximation of the matrices orthogonal to (28) and (30), see discussion at the end of Experiment 3 (Section 5.5).

## 5.5 Anisotropic reconstructions using more than 3 + 2 solutions

**Experiment 3.** Here we perform the experiment for  $\gamma_3$  (38) for which the 3+2 reconstruction algorithm fails, due to the fact that the gradient of three solutions become linearly dependent

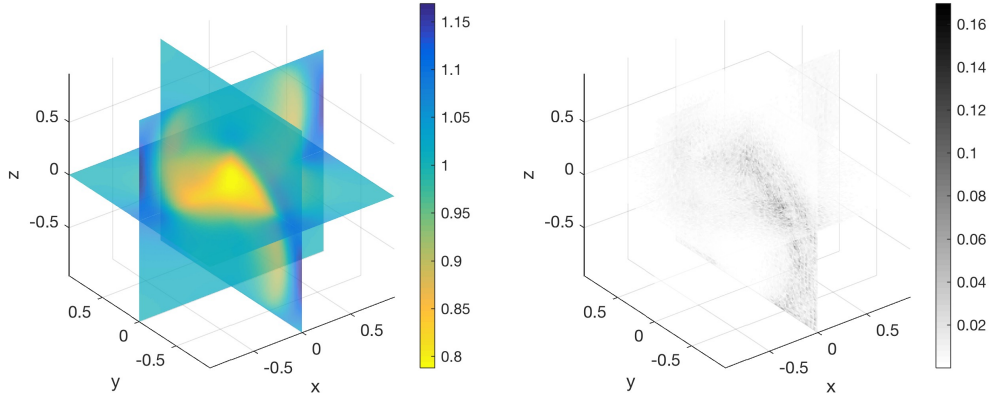


Figure 7: Exp. 2: 3D slice plot of  $\det(\nabla u_1, \nabla u_2, \nabla u_3)$  in which the computed minimum is 0.7881 (left). 3D slice plot of the error for reconstructed  $\tilde{\gamma}_2$  in relative Frobenius norm (right).

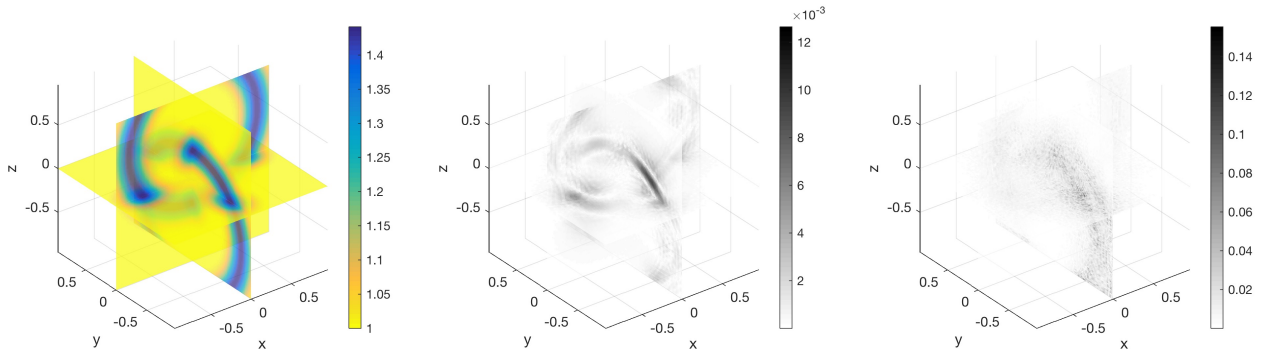


Figure 8: Exp. 2: 3D slice plots of reconstruction of  $\tau_2$  (left), relative error for  $\tau_2$  (middle) and relative error for  $\gamma_2$  in log-scale (right). The errors are in terms of the Frobenius norm.

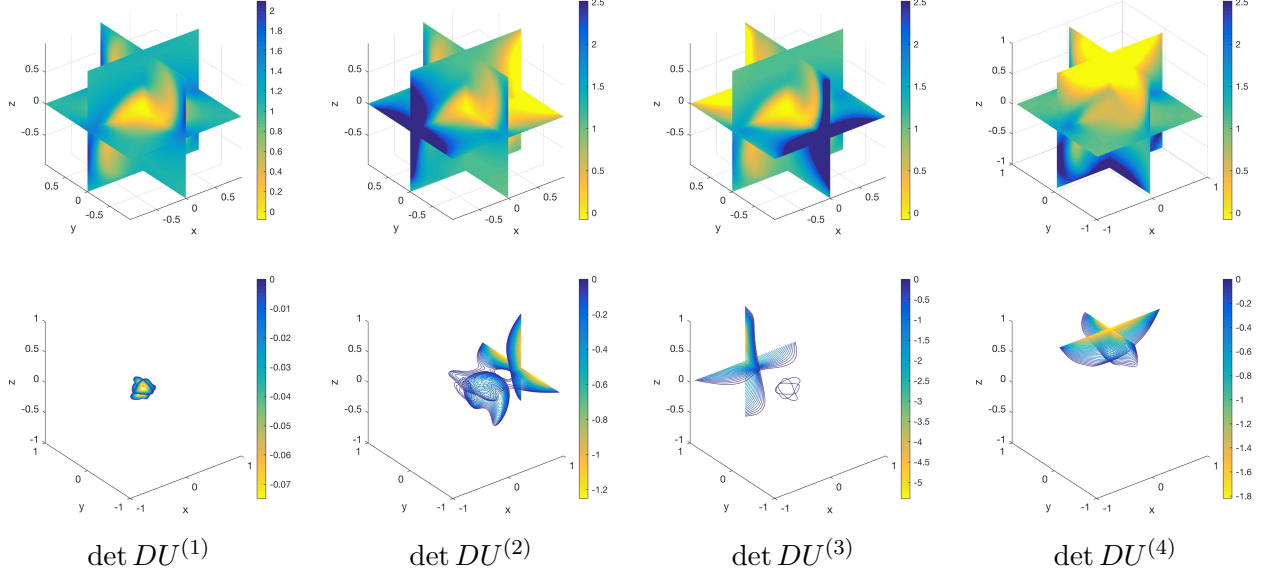


Figure 9: Exp. 3: Determinants  $\det DU^{(j)}$  for  $j = 1, 2, 3, 4$ . Top row: slice plots. Bottom row: iso-lines corresponding to the negative values.

in some parts of the domain. To overcome this difficulty, we will employ additional solutions and employ the stabilized algorithm proposed in Section 4.3. We will use the solution set  $(u_1, u_2, u_3, u_4, u_5, u_6, v_1, v_2, v_3)$  which satisfy the Dirichlet data

$$\begin{aligned}
 u_1|_{\partial X} &= x, & u_4|_{\partial X} &= x + \frac{3}{2}(z+2)^2, & v_1|_{\partial X} &= (x+2)(y+2), \\
 u_2|_{\partial X} &= y, & u_5|_{\partial X} &= y + \frac{3}{2}(x+2)^2, & v_2|_{\partial X} &= (y+2)(z+2), \\
 u_3|_{\partial X} &= z, & u_6|_{\partial X} &= z + \frac{3}{2}(y+2)^2, & v_3|_{\partial X} &= (z+2)(x+2).
 \end{aligned}$$

We will define the triples of these solutions as follows,

$$U^{(1)} := (u_1, u_2, u_3), \quad U^{(2)} := (u_4, u_2, u_3), \quad U^{(3)} := (u_1, u_5, u_3), \quad U^{(4)} := (u_1, u_2, u_6).$$

The determinant for each of these triples are then denoted

$$\begin{aligned}
 \det DU^{(1)} &= \det(\nabla u_1, \nabla u_2, \nabla u_3), & \det DU^{(2)} &= \det(\nabla u_4, \nabla u_2, \nabla u_3), \\
 \det DU^{(3)} &= \det(\nabla u_1, \nabla u_5, \nabla u_3), & \det DU^{(4)} &= \det(\nabla u_1, \nabla u_2, \nabla u_6).
 \end{aligned}$$

For each of these triples, the determinant  $\det DU^{(j)}$  vanishes and switches sign inside  $X$ , as shown in the slice plots on Fig.9. Therefore, the determinants of  $H^{(j)}$  ( $j = 1, 2, 3, 4$ ) also vanish

and the 3+2 algorithm (based on a single triple of solutions) from Section 4.2 fails. On the other hand, one may visualize on Fig.10 that the quantity

$$|\det DU^{(1)}|^2 + |\det DU^{(2)}|^2 + |\det DU^{(3)}|^2 + |\det DU^{(4)}|^2$$

is everywhere positive on  $X$  (that is, the intersection of the zero sets corresponding to the four triples is empty), setting the stage for an implementation of the stabilized algorithm.

Now one may reconstruct  $\tilde{\gamma}^{(j)}$  as in the 3+2 algorithm, for each solution triples  $U^{(j)}$  but such individual reconstructions fail locally, though never simultaneously. The choices of solutions to use for the individual 3+2 algorithms are,

$$\begin{aligned} U^{(1)} &= (u_1, u_2, u_3) & \text{with} & \quad (v_1, v_2), \\ U^{(2)} &= (u_4, u_2, u_3) & \text{with} & \quad (v_2, v_3), \\ U^{(3)} &= (u_1, u_5, u_3) & \text{with} & \quad (v_1, v_2), \\ U^{(4)} &= (u_1, u_2, u_6) & \text{with} & \quad (v_2, v_3). \end{aligned}$$

The individual errors are shown in Fig.11. However, when they are combined in the system (33) one can successfully recover the scaling  $\tau_3$ , as shown in Fig.13.

For reconstruction of  $\tilde{\gamma}_3$ , one may weight each individual reconstructions  $\tilde{\gamma}^{(j)}$  by  $|H^{(j)}|$ ,

$$\tilde{\gamma}_{3,H} := \frac{|H^{(1)}|\tilde{\gamma}^{(1)} + |H^{(2)}|\tilde{\gamma}^{(2)} + |H^{(3)}|\tilde{\gamma}^{(3)} + |H^{(4)}|\tilde{\gamma}^{(4)}}{\det (|H^{(1)}|\tilde{\gamma}^{(1)} + |H^{(2)}|\tilde{\gamma}^{(2)} + |H^{(3)}|\tilde{\gamma}^{(3)} + |H^{(4)}|\tilde{\gamma}^{(4)})^{1/3}}. \quad (41)$$

On the other hand, we observe numerically that the errors for the individual  $\tilde{\gamma}^{(j)}$ 's are inversely proportional to  $\|\tilde{\gamma}^{(j)}\|_F$ . An intuitive argument for this is that the orthogonalization to compute  $B'$  (see Step A in Section 4.2 or its stabilized equivalent Step A' in Section 4.3) corresponds more naturally to the Frobenius norm. Hence  $B'$  is most accurate when normalized in this norm, and hence whenever the reconstructed approximation to  $\tilde{\gamma}^{(j)}$  has a large Frobenius norm  $\|\tilde{\gamma}^{(j)}\|_F$ , one may expect a large error. To exploit this observation, we first choose to exclude the approximation among  $\{\tilde{\gamma}^{(j)}\}$  that has the largest Frobenius norm. To this end, we first define the spatially dependent index set

$$\mathcal{J}(x) = \{1, 2, 3, 4\} \setminus \operatorname{argmax}_i \{\|\tilde{\gamma}^{(i)}(x)\|_F\}. \quad (42)$$

Then, we define the approximation  $\tilde{\gamma}_{3,F}$  using the weighted sum of the remaining members of  $\{\tilde{\gamma}^{(j)}\}$ ,

$$\tilde{\gamma}_{3,F}(x) := \sum_{j \in \mathcal{J}(x)} \frac{\tilde{\gamma}^{(j)}}{\|\tilde{\gamma}^{(j)}\|_F} \bigg/ \det \left( \sum_{j \in \mathcal{J}(x)} \frac{\tilde{\gamma}^{(j)}}{\|\tilde{\gamma}^{(j)}\|_F} \right)^{1/3}. \quad (43)$$

This approximation yields an improvement over (41).

	$\tilde{\gamma}_{3,H}$	$\tilde{\gamma}_{3,F}$	$\tau_3$	$\gamma_3$
Rel. $L^1$ error	0.03778109	0.03233641	0.00151633	0.05352633
Rel. $L^2$ error	0.08114189	0.07685639	0.00393286	0.10300765
Rel. $L^\infty$ error	2.48883708	0.73548767	0.08635811	0.73512348
Max. pointwise rel. error	10.93893332	1.40606227	0.11662169	1.39683706

Table 3: Exp. 3: Summary of reconstruction error for  $\gamma_3$  (38). The error for the tensor-valued functions computed pointwise by the Frobenius norm, and  $\gamma_3 = \tau_3 \tilde{\gamma}_{3,F}$ .

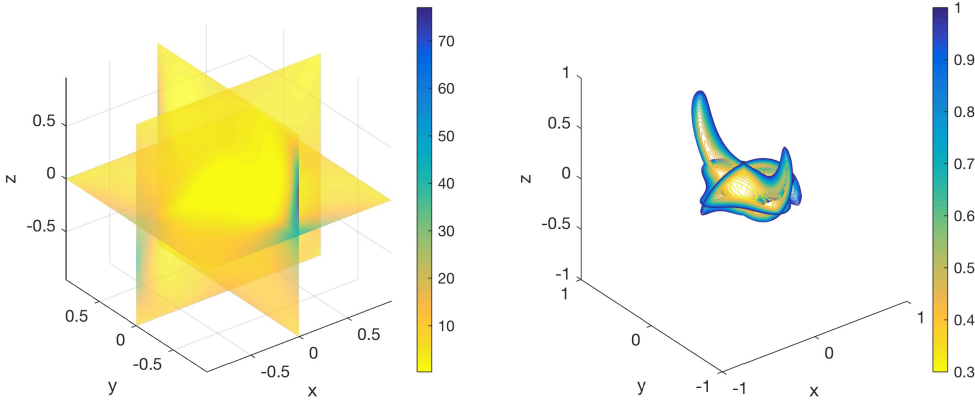


Figure 10: Exp. 3: 3D slice plot of  $\sum_{j=1}^4 |\det DU^{(j)}|^2$  (left) and 3D contour slice plot near its minimum (right). Computed minimum is 0.2981.

The full reconstruction for  $\gamma_3$  is then achieved by  $\tau_3 \tilde{\gamma}_{3,F}$ . The errors from both reconstructions are summarized in Table 3. The relative  $L^1$  error for  $\gamma_3$  is at 5% and pointwise relative error is less than 139%. The volume of the domain that incurs pointwise relative error larger than 50% is 0.03%, so here the error is highly localized, as was the case in Experiment 2. Figure 12 compares the relative errors between  $\tilde{\gamma}_{3,F}$  and  $\tilde{\gamma}_{3,H}$ . The weighting (43) significantly improves the error, numerically illustrating that the Frobenius norm serves as a good estimator of the accuracy of the anisotropic part.

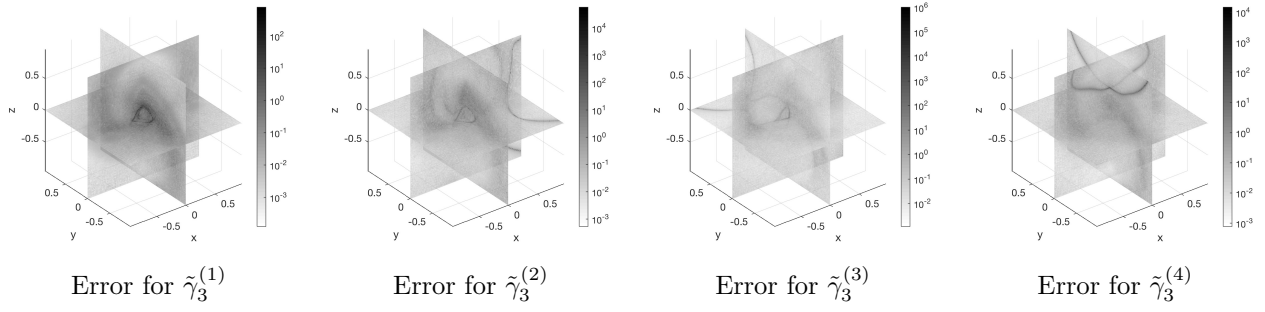


Figure 11: Exp. 3: Reconstruction error for  $\tilde{\gamma}_3^{(j)}$  ( $j = 1, 2, 3, 4$ ) measured in Frobenius norm in log-scale.

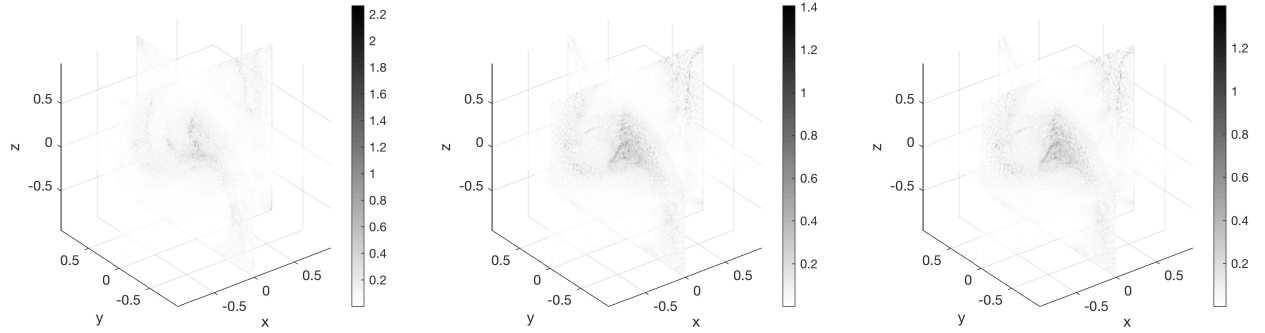


Figure 12: Exp. 3: Error for reconstruction of  $\tilde{\gamma}_3$  measured in Frobenius norm. The error for  $\tilde{\gamma}_{3,H}$  with weighting by  $\det H^{(j)}$  as in (41) (left), and for  $\tilde{\gamma}_{3,F}$  with weighting by  $1/\|\tilde{\gamma}_3^{(j)}\|_F$  as in (43) (middle), and relative error for  $\gamma_3$  (right).

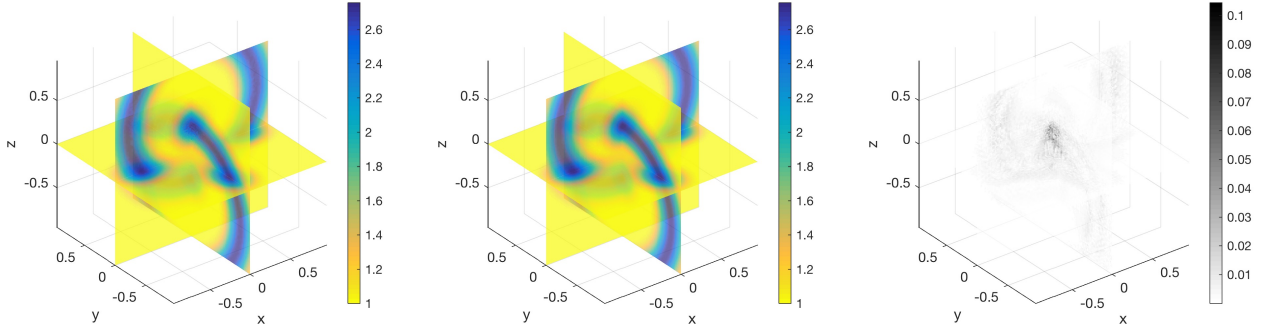


Figure 13: Exp. 3: Reconstruction of  $\tau_3$  (left), true  $\tau_3$  (middle), and relative error for the reconstruction in log-scale (right).

## 6 Conclusion

We have presented two reconstruction approaches confirming the appeal of power density functionals for the purpose of reconstructing isotropic and anisotropic conductivity tensors.

The first approach, aimed at reconstructing an isotropic conductivity, uses power densities associated with 3 conductivity solutions, and solves a local dynamical system for a quaternion-valued function, followed by a Poisson problem for the conductivity  $\sigma$ . Note that one could also solve for  $\sigma$  by integrating (17) along curves, though the Poisson equation (18) presents the advantage of projecting out the curl part of the right-hand-side of (17) before resolution.

The second approach consists in exploiting power densities of at least 5 solutions to produce pointwise reconstruction methods for anisotropic conductivities. In addition, the data surplus (compared to the first scenario) allows to bypass the “dynamical” step of the first approach, even for the purpose of reconstructing the unknown scalar factor at the end. While such reconstruction methods rely on conditions which may fail locally, we have successfully and efficiently circumvented this issue by exploiting redundancies associated with additional solutions, and avoiding the burden of keeping track of which subset of solutions satisfies the reconstructibility conditions locally. The **stabilized 3+2 algorithm** presented is “stabilized” in the sense that the instabilities caused by vanishing determinants, a phenomenon which may or may not be avoided in theory, can be circumvented in practice.

Numerical experiments (Section 5) demonstrate that the introduced algorithms (Sections 3 and 4) are able to reconstruct isotropic and anisotropic conductivities, from noiseless data. In particular, results from Experiment 3 illustrates that a global reconstruction of an anisotropic conductivity that fails to satisfy Hypothesis 4.2 can be reconstructed via the stabilized 3+2 algorithm under the relaxed conditions given by Hypothesis 4.4.

A number of detailed investigations, such as the effect of noisy data, use of various regular-

izations, and further improvements to the algorithms will be investigated in future work.

## References

- [1] G. S. ALBERTI, G. BAL, AND M. DI CRISTO, *Critical points for elliptic equations with prescribed boundary conditions*, (2016). arXiv:1611.06989. [2](#), [4](#)
- [2] G. ALESSANDRINI AND V. NESI, *Univalent  $e^\sigma$ -harmonic mappings*, Arch. Rat. Mech. Anal., 158 (2001), pp. 155–171. [4](#)
- [3] G. ALESSANDRINI AND V. NESI, *Quantitative estimates on jacobians for hybrid inverse problems*, Bulletin of South Ural State University. Series: Mathematical modeling and programming, 8 (2015). [2](#)
- [4] H. AMMARI, E. BONNETIER, Y. CAPDEBOSCQ, M. TANTER, AND M. FINK, *Electrical Impedance Tomography by elastic deformation*, SIAM J. Appl. Math., 68 (2008), pp. 1557–1573. [2](#)
- [5] S. ARRIDGE AND O. SCHERZER, *Imaging from coupled physics*, Inverse Problems, 28 (2012), p. 080201. [1](#)
- [6] G. BAL, *Cauchy problem for Ultrasound Modulated EIT*, Analysis & PDE, 6 (2013), pp. 751–775. [21](#)
- [7] G. BAL, *Hybrid inverse problems and internal functionals*, Inverse problems and applications: inside out. II, 60 (2013), pp. 325–368. [1](#)
- [8] G. BAL, C. BELLIS, S. IMPERIALE, AND F. MONARD, *Reconstruction of constitutive parameters in isotropic linear elasticity from full-field measurements*, Inverse Problems, 30 (2014), p. 125004. [2](#)
- [9] G. BAL, E. BONNETIER, F. MONARD, AND F. TRIKI, *Inverse diffusion from knowledge of power densities*, Inverse Problems and Imaging, 7 (2013), pp. 353–375. [1](#), [2](#), [3](#), [5](#), [6](#)
- [10] G. BAL AND M. COURDURIER, *Boundary control of elliptic solutions to enforce local constraints*, Journal of Differential Equations, 255 (2013), pp. 1357–1381. [2](#)
- [11] G. BAL, C. GUO, AND F. MONARD, *Imaging of anisotropic conductivities from current densities in two dimensions*, SIAM J. on Imaging Sciences, 7 (2014), pp. 2538–2557. [2](#)
- [12] ———, *Inverse anisotropic conductivity from internal current densities*, Inverse Problems, 30 (2014), p. 025001. [2](#)

- [13] ———, *Linearized internal functionals for anisotropic conductivities*, *Inv. Probl. and Imaging*, 8 (2014), pp. 1–22. [2](#), [3](#), [4](#)
- [14] G. BAL, F. MONARD, AND G. UHLMANN, *Reconstruction of a fully anisotropic elasticity tensor from knowledge of displacement fields*, *SIAM J. Appl. Math.*, 75 (2015), pp. 2214–2231. [2](#)
- [15] G. BAL, W. NAETAR, O. SCHERZER, AND J. SCHOTLAND, *The levenberg-marquardt iteration for numerical inversion of the power density operator*, *J. Inv. Ill-Posed Problems*, 21 (2013), p. 265280. [2](#)
- [16] M. BAČÁK, R. BERGMANN, G. STEIDL, AND A. WEINMANN, *A second order nonsmooth variational model for restoring manifold-valued images*, *SIAM Journal on Scientific Computing*, 38 (2016), pp. A567–A597. [20](#)
- [17] C. BELLIS AND H. MOULINEC, *A full-field image conversion method for the inverse conductivity problem with internal measurements*, in *Proc. R. Soc. A*, vol. 472, The Royal Society, 2016, p. 20150488. [2](#)
- [18] D. BRAESS, *Finite Elements: Theory, Fast Solvers, and Applications in Solid Mechanics*, Cambridge University Press, 3 ed., 2007. [21](#)
- [19] BRIANE, MILTON, AND V. NESI, *Change of sign of the correctors determinant for homogenization in three-dimensional conductivity*, *Arch. Rat. Mech. Anal.*, 173 (2004), pp. 133–150. [21](#)
- [20] Y. CAPDEBOSCQ, *On a counter-example to quantitative jacobian bounds*, *Journal de l'École polytechnique Mathématiques*, 2 (2015), pp. 171–178. [2](#), [4](#)
- [21] Y. CAPDEBOSCQ, J. FEHRENBACH, F. DE GOURNAY, AND O. KAVIAN, *Imaging by modification: Numerical reconstruction of local conductivities from corresponding power density measurements*, *SIAM Journal on Imaging Sciences*, 2 (2009), pp. 1003–1030. [2](#), [4](#)
- [22] E. DEĞIRMENCI AND B. M. EYÜBOĞLU, *Anisotropic conductivity imaging with mreit using equipotential projection algorithm*, *Physics in Medicine and Biology*, 52 (2007), p. 7229. [2](#)
- [23] G. DI FAZIO, E. FRANCI, F. RACITI, AND S. VESSELLA, *Stable determination of a lamé coefficient by one internal measurement of displacement*, *Journal of Mathematical Analysis and Applications*, 452 (2017), pp. 388–400. [2](#)
- [24] B. GEBAUER AND O. SCHERZER, *Impedance-Acoustic Tomography*, *SIAM J. Applied Math.*, 69 (2009), pp. 565–576. [2](#)
- [25] K. HOFFMANN AND K. KNUDSEN, *Iterative reconstruction methods for hybrid inverse problems in impedance tomography*, *Sensing and Imaging*, 15 (2014). [2](#)

- [26] I. KOCYIGIT, *Acousto-electric tomography and cgo solutions with internal data*, Inverse Problems, 28 (2012), p. 125004. [2](#)
- [27] R.-Y. LAI, *Uniqueness and stability of lamé parameters in elastography*, Journal of Spectral Theory, 4 (2014), pp. 841–877. [2](#)
- [28] R. LEVEQUE, *Finite Difference Methods for Ordinary and Partial Differential Equations*, Society for Industrial and Applied Mathematics, 2007. [21](#)
- [29] F. MONARD, *Taming unstable inverse problems. Mathematical routes toward high-resolution medical imaging modalities*, PhD thesis, Columbia University, 2012. [3](#), [11](#)
- [30] F. MONARD AND G. BAL, *Inverse anisotropic diffusion from power density measurements in two dimensions*, Inverse Problems, 28 (2012), p. 084001. [2](#), [3](#), [4](#)
- [31] ———, *Inverse diffusion problems with redundant internal information*, Inv. Probl. Imaging, 6 (2012), pp. 289–313. [2](#), [3](#), [4](#), [6](#)
- [32] ———, *Inverse anisotropic conductivity from power densities in dimension  $n \geq 3$* , Comm. PDE, 38 (2013), pp. 1183–1207. [1](#), [2](#), [3](#), [4](#), [5](#), [11](#), [14](#)
- [33] F. MONARD AND D. RIM, *Code archive*, 2017. [doi:10.5281/zenodo.1127682](https://doi.org/10.5281/zenodo.1127682). [18](#)
- [34] C. MONTALTO AND A. TAMASAN, *Stability in conductivity imaging from partial measurements of one interior current*, Inverse Problems and Imaging, 11 (2017), pp. 339–353. [2](#)
- [35] A. NACHMAN, A. TAMASAN, AND A. TIMONOV, *Recovering the conductivity from a single measurement of interior data*, Inverse Problems, 25 (2009), p. 035014. [2](#)
- [36] A. NACHMAN, A. TAMASAN, AND A. TIMONOV, *Current density impedance imaging*, AMS series in Contemporary Mathematics, 559 (2011). [2](#)
- [37] J. STUELPNAGEL, *On the parametrization of the three-dimensional rotation group*, SIAM Review, 6 (1964). [2](#)
- [38] D. YAN, W. XU, J. LI, ET AL., *Anisotropic wm conductivity reconstruction based on diffusion tensor magnetic resonance imaging: a simulation study*, Journal of Biomedical Science and Engineering, 3 (2010), p. 776. [2](#)